The phase response of a rough rectangular facet for radar sounder simulations of both coherent and incoherent scattering

C. Gerekos[1], M. S. Haynes[2], D. M. Schroeder[3], D. D. Blankenship[1]

[1]Institute for Geoscience, University of Texas at Austin, Texas, USA
[2]Jet Propulsion Laboratory, California Institute of Technology, California, USA
[3]Department of Geophysics and Electrical Engineering, Stanford University, California, USA

Key Points:

- Planetary digital elevation models are often of coarse resolution and depict a surface that is smooth at scales below that resolution.
- Polynomial phase approximations can be used to simulate radar scattering rigorously but they overestimate the coherence of reflected signals.
- We analytically derive the linear phase approximation formula on a rough rectangular facet, leading to much better clutter simulations.

Corresponding author: Christopher Gerekos, `christopher.gerekos@austin.utexas.edu`

Abstract

With radar sounders, coherent backscattering simulations from global planetary DEMs typically display a deficit in diffuse clutter, which is mainly due to the implicit assumption that roughness at scales below the resolution of the DEM is absent. Indeed, while polynomial approximations of the phase evolution across the facet allow for fast and mathematically rigorous simulators, the coarse resolution of these planetary DEMs leads to a potentially significant portion of the backscattering response being neglected. In this paper, we derive the analytical phase response of a rough rectangular facet characterised by Gaussian roughness and a Gaussian isotropic correlation function under the linear phase approximation. Formulae for the coherent and incoherent power scattered by such an object are obtained for arbitrary bistatic scattering angles. Validation is done both in isolation and after inclusion in different Stratton-Chu simulators. In order to illustrate the different uses of such a formulation, we reproduce two lunar radargrams acquired by the LRS instrument with a Stratton-Chu simulator incorporating the proposed rough facet phase integral, and we show that the original radargrams are significantly better-reproduced than with state-of-the-art methods, at a similar computational cost. We also show how the rough facet integral formulation can be used in isolation to better characterise subglacial water bodies on Earth.

1 Introduction

Radar sounders are low-frequency, nadir-pointing remote sensing instruments that operate by recording and processing electromagnetic signals reflected from a planetary body of interest. The incoming waveform that generates these reflections is generally transmitted by the radar sounder itself, a mode of operation known as active sounding, although signals of opportunity may also be used, a mode of operation known as passive sounding (Ulaby et al., 1981). Since the amplitude and phase of these reflections correspond to given changes of the dielectric constant across the medium of propagation, it is possible to infer a great amount of information from analysing these signals. For instance, radar sounders can be sensitive to the presence and composition of possible subsurface features (Ulaby et al., 1981).

In the last two decades, three highly successful orbital radar sounders have been operated within the Solar System: the Mars Advanced Radar for Subsurface and Ionosphere Sounding (MARSIS) instrument aboard the the European Space Agency (ESA) Mars Express mission (Jordan et al., 2009); the Shallow Radar (SHARAD) instrument aboard the US National Aeronautics and Space Administration (NASA) Mars Reconnaissance Orbiter (MRO) mission (Croci et al., 2011); and the Lunar Radar Sounder (LRS) instrument aboard the Japan Aerospace Exploration Agency (JAXA) *Kaguya* mission (Ono et al., 2010). Three major planetary science missions embarking radar sounders are currently under development: the Radar for Icy Moons Exploration (RIME) of the ESA Jupiter Icy Moons Explorer (JUICE) spacecraft (Bruzzone et al., 2013); the Radar for Europa Assessment and Sounding: Ocean to Near-surface (REASON) instrument on the NASA Europa Clipper spacecraft (Blankenship et al., 2018); and the Subsurface Radar Sounder (SRS) aboard ESA's Envision mission to Venus (Bruzzone et al., 2020).

On Earth, airborne radar sounding of terrestrial ice sheets is one of the primary geophysical tools for characterising subglacial hydrologic systems (Schroeder et al., 2020). This includes studies that range from mapping the distribution of subglacial lakes across entire ice sheets (Wright & Siegert, 2012) to investigating the onset of subglacial melting within a glacier catchment (Chu et al., 2018) and analysing individual water subglacial bodies (Rutishauser et al., 2018).

Coherent backscattering simulators are tools of central importance at all stages of a radar sounder mission. They can assist in the design and validation of the instrument, help validate processing algorithms, and can also support planning and post-acquisition

analysis of the data. Such simulators take as input the characteristics of the instrument, of its environment, and a discretised version of the terrain of interest, or *digital eleva-tion model* (DEM), and give as output the radar response of the terrain for the consid-ered instrument. There are different types of backscattering simulators applied to radar sounding, the most important ones being finite-difference time-domain (FDTD) algorithms (Heggy et al., 2017), method of moments (MoM) simulators, pseudospectral methods (Lei et al., 2020), and those based on the Stratton-Chu formula (Berquin et al., 2015; Fa & Jin, 2010; Gerekos et al., 2018; Kobayashi et al., 2002; Nouvel et al., 2004).

A common issue in planetary remote sensing is that global DEMs of Solar Systems objects usually have poor resolutions, in the hundreds of metres, whereas most backscat-tering simulation methods demand a resolution of the order of a tenth of the wavelength of the instrument, *i.e.*, typically of the order of the metre, in order to be mathematically accurate. Stratton-Chu-type methods typically require more assumptions about scat-tering, but have been particularly popular in radar science due to their efficiency. These methods combine a way to compute the amplitude and polarisation of a field on a facet with a way to compute its phase. By allowing linear or polynomial variations of the phase across the facets of the DEM, it is possible to allow facets as large as several times the wavelength of the instruments (Berquin et al., 2015; Nouvel et al., 2004) – a huge com-putational improvement over FDTD or MoM simulators, which require an important over-sampling of the DEM to respect their internal assumptions. The large-facet linear phase approximation has been solved analytically for square (Nouvel et al., 2004) and trian-gular facets (Berquin et al., 2015), and has been generalised to multilayer terrains (Gerekos et al., 2018).

However, even a well-crafted simulator is typically only as good as the input DEM, and a major limitation of having poorly-resolved DEMs is that roughness at scales be-low the resolution of the DEM is effectively taken to be zero (see Figure 1). However, this small-scale roughness is present on the real terrain and has a significant effect on the radar response, typically decreasing the nadir response and heightening the diffuse off-nadir response, both being a disadvantage for subsurface radar sounding. These ef-fects cannot be seen in a simulation based on a coarsely-resolved DEM, leading to a sim-ulated response that is "too coherent", that is, with an excess of specular power and an underestimation of non-specular power (Berquin et al., 2015; Gerekos et al., 2018). Find-ing a way to include this small-scale response in Stratton-Chu simulators based on the linear phase approximation is thus crucial to fully benefit from these efficient methods. We note that similar problems have been looked at, with different assumptions and con-texts, in the Global Navigation Satellite System Reflectometry (GNSS-R) and high-resolution synthetic aperture radar (SAR) communities (Dente et al., 2020; Xu et al., 2021), although none of these formulations is entirely applicable to our problem. Within radar sounders specifically, (Grima, Schroeder, et al., 2014) derives the backscattered power from a fi-nite rough ellipse under the small perturbation model, but using rudimentary assump-tions on scattering. We also note that Sbalchiero et al. (2021) propose a treatment of a reduced version of this problem (*i.e.*, using the discrete Stratton-Chu formula with rough facets) using FDTD pre-computed responses, but to our knowledge, the problem has yet to be solved analytically and validated for full radar responses.

In this paper, we propose to generalise the linear phase approximation to rough rect-angular facets. Starting from the fundamental equation that describes the evolution of phase across a surface, we analytically recompute the integral of Nouvel et al. (2004) on a perturbed facet (see Figure 2), which is defined statistically. Separating the mean and the variance of the resulting power, a "coherent" and "incoherent" term naturally emerge. The formula for the phase response of a rough facet is rigorously validated both in iso-lation and integrated in Stratton-Chu simulators. After characterising and validating our formula, we show two different applications. The first is forward modelling. We illustrate our integrated all-scale simulator by reproducing LRS radargrams over two different re-

gions on the Moon, a mare and a crater, with and without the rough facet phase formula. The second application is to characterise subglacial water bodies using an updated version of the model described in Schroeder et al. (2014a). This application uses the rough facet integrals on their own, and does not involve a Stratton-Chu simulator.

Our paper is structured as follows. In Section 2, we recall the state of the art in Stratton-Chu simulators and the linear phase approximation. In Section 3 we present our derivation of the comprehensive phase response of a rough facet. In Section 4 we present the validation of our formula from two different perspectives. Section 5 presents the two different applications of the rough facet phase integral. Section 6 concludes the paper.

2 State of the art in large-facet coherent simulators

Let us consider a discrete scatterer at a position $\mathbf{r}'$. The phase accumulated by a plane wave travelling from an emission point $\mathbf{r_i}$ to $\mathbf{r}'$ and then reflected or transmitted from $\mathbf{r}'$ to a reception point $\mathbf{r_r}$ will be given by

$$\phi(\mathbf{r_i}, \mathbf{r_r}, \mathbf{r}') = e^{i(k_i|\mathbf{r}'-\mathbf{r_i}|+k_s|\mathbf{r_r}-\mathbf{r}'|)}, \tag{1}$$

where $\mathbf{k_i} \equiv k_i\hat{\mathbf{k}}_\mathbf{i}$ and $\mathbf{k_s} \equiv k_s\hat{\mathbf{k}}_\mathbf{s}$ are the incoming and scattering wavevectors, respectively. In the case of a transmission, $\mathbf{k_i}$ and $\mathbf{k_s}$ have different norms, due to the change of dielectric constant at the interface. In the case of a reflection, their norms are the same. Finally, in the case of a monostatic reflection, *i.e.*, when the receiver and the emitter are located at the same place, $\mathbf{k_i}$ and $\mathbf{k_s}$ have identical norms and opposite signs.

Let us now consider that the scatterer is a facet, *i.e.*, a continuous, smooth surface A of initially arbitrary shape. In this case, the phase of the received signal will be given by the integral of the expression above over the surface of this facet (see Figure 2-left):

$$\Phi(\mathbf{r_r}, \mathbf{r_i}) = \oiint_A \phi(\mathbf{r_i}, \mathbf{r_r}, \mathbf{r}')d\mathbf{r}'. \tag{2}$$

If the dimensions of the facets are very small, typically of the order of $\lambda/10$, it is reasonable to consider that the phase (1) is constant across the facet, in which case the integral (2) is trivially solved: $\Phi(\mathbf{r_r}, \mathbf{r_i}) = \mathcal{A}e^{i(k_i|\mathbf{r}_\alpha-\mathbf{r_i}|+k_s|\mathbf{r_r}-\mathbf{r}_\alpha|)}$, where $\mathcal{A}$ is the area of facet A and $\mathbf{r}_\alpha$ an arbitrarily-chosen point on its surface, typically its geometrical centre. This method is known as the *constant phase approximation* (CPA) (Berquin et al., 2015). The main drawback of this approximation is that, for planetary DEMs with resolutions of hundreds of metres, it requires massive amounts of oversampling to reach the $\mathcal{O}(\lambda/10)$ criterion.

For this reason, more advanced phase computation methods have been devised. We review them in the next subsection.

2.1 Analytical phase integrals

Let us assume that A is a planar facet lying within a plane described by the following equation:

$$\left\{\mathbf{r}'|ax' + by' + d = z'\right\}, \tag{3}$$

where x', y', and z' are the coordinates of $\mathbf{r}'$ and a, b, d are real coefficients. The linear phase approximation assumes that the argument of the exponential in (1) can be linearised in the components of $\mathbf{r}'$ as follows (Berquin et al., 2015).

$$k_i|\mathbf{r}' - \mathbf{r_i}| + k_s|\mathbf{r_r} - \mathbf{r}'| = A_0x' + B_0y' - D_0, \tag{4}$$

where

$$\begin{cases} A_0 &= k_{d,x} + ak_{d,z}, \\ B_0 &= k_{d,y} + bk_{d,z}, \\ D_0 &= (\mathbf{r_i} \cdot \mathbf{k_i} - \mathbf{r_r} \cdot \mathbf{k_s}) - dk_{d,z}, \end{cases} \tag{5}$$

Real terrain
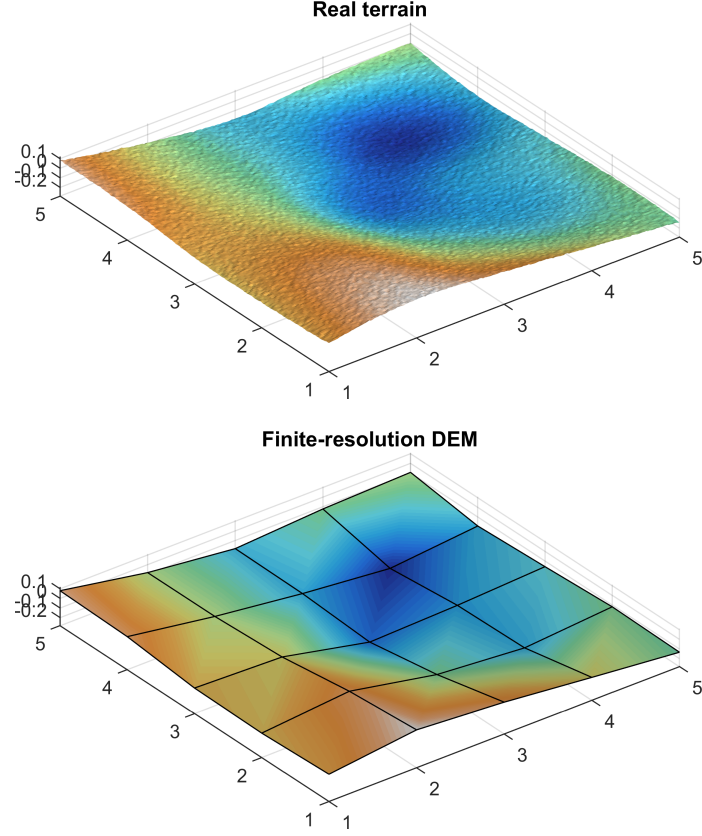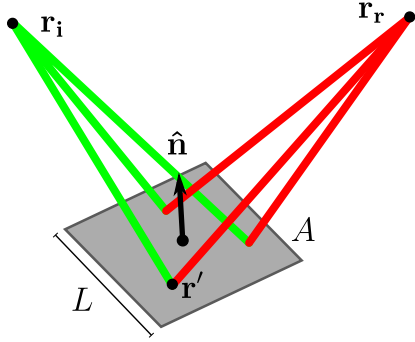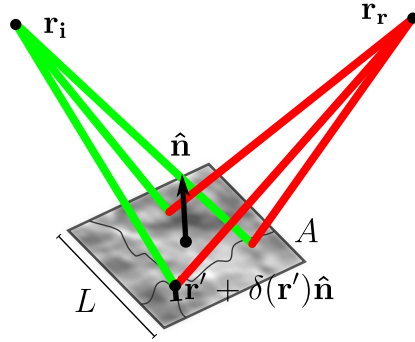
Finite-resolution DEM

Figure 1: Illustration of the differences that might exist between a real-life terrain, which is characterised by roughness down to the smallest scales (top), and a typical digital elevation model of that terrain, which is sampled at regularly-spaced intervals (bottom). Axes represent distance in arbitrary units.

Phase integral over a smooth facet (usual approach)

Phase integral over a rough facet (this work)

$$P \propto \left| \oiint_A \phi(\mathbf{r_i}, \mathbf{r_r}, \mathbf{r'}) d\mathbf{r'} \right|^2 \qquad P \propto \left| \left\langle \oiint_A \phi(\mathbf{r_i}, \mathbf{r_r}, \mathbf{r'} + \delta(\mathbf{r'})\hat{\mathbf{n}}) d\mathbf{r'} \right\rangle \right|^2$$

Figure 2: Illustration of the main quantities involved in the computation of the phase integral and resulting power. The integration variable $\mathbf{r'}$ runs over the plane defining the facet [see (3)]. If the considered facet is smooth (left), the integration is done over $\mathbf{r'}$; if it is rough (right), the integration runs over $\mathbf{r'}$ plus a perturbation $\delta(\mathbf{r'})$ that is parallel to the normal $\hat{\mathbf{n}}$.

with

$$\mathbf{k_d} \equiv \mathbf{k_i} - \mathbf{k_s}. \tag{6}$$

The integral (2) has been solved analytically in the case of square (Nouvel et al., 2004) and triangular facets (Berquin et al., 2015). In the case of a square facet of length L, the phase integral reduces to

$$\Phi(\mathbf{r_r}, \mathbf{r_i}) = e^{-iD_0} L_x L_y \operatorname{sinc}\left(\frac{L_x A_0}{2}\right) \operatorname{sinc}\left(\frac{L_y B_0}{2}\right). \tag{7}$$

where $\operatorname{sinc}(x) \equiv \sin(x)/x$ and with

$$L_x = L \cos \alpha_x, \quad L_y = L \cos \alpha_y, \tag{8}$$

where $\alpha_{x,y}$ are the x- and y-direction inclination angles of the facet, defined through $\sin \alpha_x = |\hat{n}_x|$, $\sin \alpha_y = |\hat{n}_y|$, and where $\hat{\mathbf{n}}$ is the unit outgoing (zenith-facing) normal to the facet. Formula (7) is known as the *linear phase approximation* (LPA). We note that, since any four points of a DEM generally do not generally lie on a single plane, additional assumptions must be made for the definitions of the square facet itself. Here, we use the 5-point method outlined in (Nouvel et al., 2004) to define the average plane at any given DEM point, and normal $\hat{\mathbf{n}}$ to that plane, which is used to define the coefficients $\{a, b\}$ is taken as the average of the normals obtained from each pair of edges. It should be remarked the use of square facets leads to the simulated DEM having discontinuities (consecutive facets do not necessarily share same edge orientation), a problem already noted in (Nouvel et al., 2004), and which has measurable impact on the backscattered response. This will be discussed in Section 4 when relevant.

We note that the formulation is identical for the more general case of rectangular facets, one just needs to replace L in (8) by the lengths L_1, L_2 of the facet edges.

With this expression as the phase contribution of a facet in (11), we are allowed to have $L \gtrsim \lambda$, thus saving a huge amount of computational resources. Since most planetary DEMs are indeed coarsely-sampled, this formulation is a very efficient way to simulate radar backscattering under these conditions. This formula only works inasmuch as the small variations of the direction of incoming and scattered wavevectors across the facet can be neglected. In practice it is reliable for facet lengths up to a few wavelengths. Higher-order polynomial approximations for the phase variations have been computed for cases when even larger facet sizes are required (Berquin et al., 2015; Nouvel et al., 2004). In this paper, we will limit ourselves to the linear phase approximation.

The roughness at scales smaller than the resolution of the DEM are not captured by the linear phase approximation, since formula (7) is purely deterministic and depends solely on the DEM. On a real terrain, however, smaller-scale roughness is present and its effect is measurable. Reproducing this response whilst keeping large facets –that is, without resorting to oversampling the DEM to $\lambda/10$ and adding a realisation of the small-scale roughness– is the purpose of this work.

2.2 Stratton-Chu formula

Although the phase is usually the most complicated factor to compute, one must also know the amplitude and polarisation of the electromagnetic fields in order to simulate scattering from or through a surface. The expressions above are meant to be used alongside the Stratton-Chu formula, which is based on the Kirchoff approximation, and is used to compute the complete back- or forward-scattered electric field.

It is almost always the case that the relevant quantities evolve sufficiently slowly across the surface to allow for the discretisation of that surface into facets, and to assume the field amplitudes and polarisations are constant across any given facet. In ef-

fect, we are no longer computing the scattering on a given surface, but on an approx-
imation of that surface being the DEM. Incidentally, our knowledge of the topography
of planetary bodies is also limited by the resolution of the instrument they were mea-
sured with, and are thus also discrete, or digital, objects.

In their discretised form, the Stratton-Chu formulae for backscattered and forward-
scattered electric fields are given by [see e.g. Gerekos (2020)]:

$$\mathbf{E}^{\text{refl}}(\mathbf{r_r}) = ik_i \sum_{\alpha}^{N} [\mathbf{I} - \hat{\mathbf{k}}_{\mathbf{s}} \hat{\mathbf{k}}_{\mathbf{s}}] \cdot [Z_i \mathbf{H}_{\parallel}(\mathbf{r}_\alpha) + \hat{\mathbf{k}}_{\mathbf{s}} \times \mathbf{E}_{\parallel}(\mathbf{r}_\alpha)] \Phi_\alpha(\mathbf{r_r}, \mathbf{r_i}), \tag{9}$$

$$\mathbf{E}^{\text{trans}}(\mathbf{r_r}) = -ik_s \sum_{\alpha}^{N} [\mathbf{I} - \hat{\mathbf{k}}_{\mathbf{s}} \hat{\mathbf{k}}_{\mathbf{s}}] \cdot [Z_r \mathbf{H}_{\parallel}(\mathbf{r}_\alpha) + \hat{\mathbf{k}}_{\mathbf{s}} \times \mathbf{E}_{\parallel}(\mathbf{r}_\alpha)] \Phi_\alpha(\mathbf{r_r}, \mathbf{r_i}), \tag{10}$$

where α represents the index of the considered facet and N the number of considered
facets. Z_i and Z_r are the impedances of the medium of transmission and reception, re-
spectively. $\hat{\mathbf{k}}_{\mathbf{s}} \equiv (\mathbf{r_r} - \mathbf{r}_\alpha)|\mathbf{r_r} - \mathbf{r}_\alpha|^{-1}$ is the scattering vector and also depends on α.
$\mathbf{E}_{\parallel}$ and $\mathbf{H}_{\parallel}$ are the parallel components of the incoming electric and magnetic fields. $\mathbf{I}$
is the identity tensor. Lastly, Φ_α is the phase integral over the facet A_α defined in (2).

To keep notation more succinct, it is common to regroup all the non-phase factors
into a single object, and write

$$\mathbf{E}(\mathbf{r_r}) = \sum_{\alpha}^{N} \mathbf{F}_\alpha(\mathbf{r_r}, \mathbf{r_i}) \Phi_\alpha(\mathbf{r_r}, \mathbf{r_i}). \tag{11}$$

In the following, the α indices may be dropped for clarity. When the vector nature
of the problem is not relevant, the electric field may be written as a scalar E and the cor-
responding Stratton-Chu factors as F.

2.3 Stratton-Chu formula with a time-domain signal

The expressions above are in principle only valid for monochromatic fields. To in-
clude time-dependence, one should recompute the scattered field for all frequencies in-
volved and recombine them with appropriate weights through a Fourier transform. How-
ever, this process can be bypassed in the case of radar sounders due to their narrow band-
width, in which case the facet response in phase, delay and amplitude is computed at
the centre frequency f_0 only (Gerekos et al., 2018, 2019). In this case we consider that
each facet reflects a delayed copy of the incoming signal $s(t)$, and the time-dependant
Stratton-Chu formula then reads :

$$\mathbf{E}(\mathbf{r_r}, t) \approx \sum_{\alpha}^{N} \mathbf{F}_\alpha(\mathbf{r_r}, \mathbf{r_i})\big|_{f=f_0} \Phi_\alpha(\mathbf{r_r}, \mathbf{r_i})\big|_{f=f_0} s(t - \tau_\alpha), \tag{12}$$

where τ_α is the travel time of the signals from the emitter to the facet centre to the re-
ceiver.

To keep notation light, time-dependence will not be shown explicitly unless nec-
essary.

3 Phase response of a rough facet

We now aim at analysing how (7) changes when the planar surface of the facet is
perturbed. The first steps of the derivation of the facet-level rough phase integral, the
main novel contribution of this paper, partially follow those of (Fung, 1994; Kong, 2000;
Tsang & Kong, 2004) on the backscattering law of an infinite random rough terrain un-
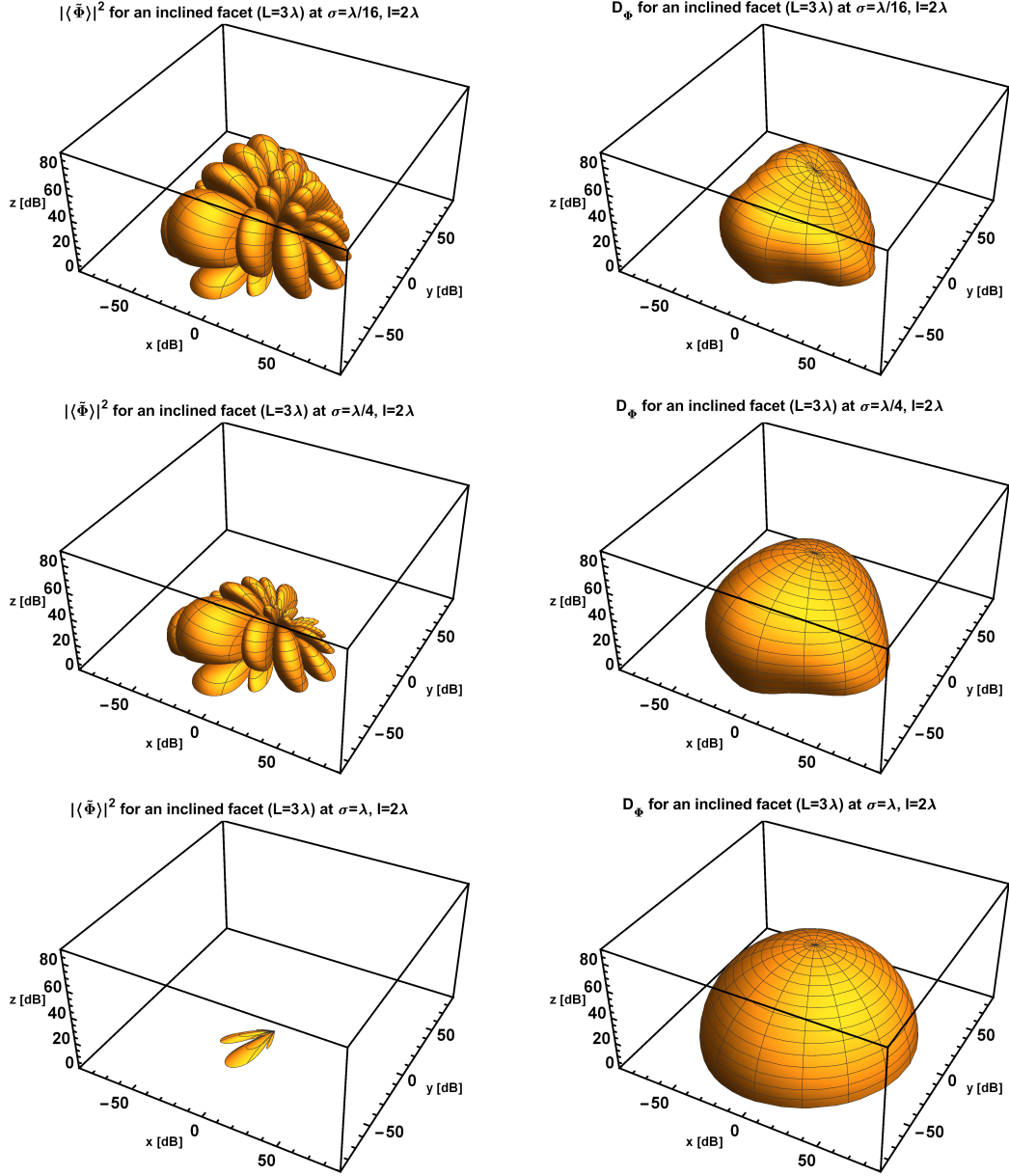der the Kirchoff approximation, which we adapt here for continuity.

Figure 3: Graph of the functions $|\langle\tilde{\Phi}\rangle|^2$ (left) and D_Φ (right) for a facet of length $L = 3\lambda$ that lies on the plane defined by the equation $-0.2x - 0.5y = z$. Roughness in top row: $\sigma = \lambda/16$; middle row: $\sigma = \lambda/4$, and bottom row: $\sigma = \lambda$, all of which with $l = 2\lambda$. The emitter is located at $\mathbf{r_i} = (0, 0, 2000\lambda)$, and points towards nadir: $\hat{\mathbf{k}}_i = (0, 0, -1)$. The bounds of the box are equal to L^4, the theoretical maximum of the square norm of the phase integral for any given direction.

3.1 Definition of the perturbation

As in Kong (2000), we add a perturbation to the surface of the facet in a direction parallel to the normal of that facet

$$\mathbf{r}' \to \mathbf{r}' + \delta(\mathbf{r}')\hat{\mathbf{n}}, \tag{13}$$

where $\delta(\mathbf{r}') \sim \mathcal{N}(0, \sigma^2)$ is a zero-mean Gaussian perturbation of variance σ^2 (see Figure 2-right). Moreover, we assume an isotropic Gaussian correlation function for the rough facet, and we denote l its correlation length.

We now perform a Taylor expansion on $|\mathbf{r}-(\mathbf{r}'+\delta(\mathbf{r}')\hat{\mathbf{n}})|$ around the small quantity $\delta(\mathbf{r}')$, also called the vector modulus approximation by some authors: $|\mathbf{r}-(\mathbf{r}'+\delta(\mathbf{r}')\hat{\mathbf{n}})| = |\mathbf{r}-\mathbf{r}'| - \hat{\mathbf{n}}\cdot(\mathbf{r}-\mathbf{r}')|\mathbf{r}-\mathbf{r}'|^{-1}\delta(\mathbf{r}') + \mathcal{O}(\delta^2)$. Thus under the perturbation the phase (1) becomes

$$\phi \to \tilde{\phi} = \phi e^{-iK\delta(\mathbf{r}')}, \tag{14}$$

with

$$K \equiv k_i \cos\theta_i + k_s \cos\theta_r, \tag{15}$$

and where $\cos\theta_i = \hat{\mathbf{n}}\cdot(\mathbf{r_i}-\mathbf{r}')|\mathbf{r_i}-\mathbf{r}'|^{-1}$ and $\cos\theta_r = \hat{\mathbf{n}}\cdot(\mathbf{r_r}-\mathbf{r}')|\mathbf{r_r}-\mathbf{r}'|^{-1}$. Since the angles θ_i and θ_r vary very little over the facet, we will replace $\mathbf{r}'$ by $\mathbf{r}_\alpha$ in the cosine formulae, thus making K independent of $\mathbf{r}'$.

3.2 Total perturbed intensity

We now show how to compute the total ensemble-averaged intensity $P(\mathbf{r_r}) = \langle|E(\mathbf{r_r})E^\dagger(\mathbf{r_r})|\rangle$ of the field (11) reflected by a collection of rough facets, following the derivation of Kong (2000). Without loss of generality, we write

$$P(\mathbf{r_r}) = |\langle E(\mathbf{r_r})\rangle|^2 + \left(\langle|E(\mathbf{r_r})|^2\rangle - |\langle E(\mathbf{r_r})\rangle|^2\right), \tag{16}$$

$$\equiv |E_{\text{avg}}(\mathbf{r_r})|^2 + E_{\text{var}}^2(\mathbf{r_r}), \tag{17}$$

where $E_{\text{var}}^2(\mathbf{r_r}) \equiv \langle|E(\mathbf{r_r})|^2\rangle - |\langle E(\mathbf{r_r})\rangle|^2$. In essence, we have decomposed the field into an average part and a fluctuating part. The power of the average part adds coherently (and is thus referred to as the coherent power) while the power from the fluctuating term adds incoherently (and is thus referred to as the incoherent power) (Campbell & Shepard, 2003). In other words we can write:

$$|E_{\text{avg}}(\mathbf{r_r})|^2 = \left|\sum_\alpha^N F_\alpha(\mathbf{r_i}, \mathbf{r_r})\langle\tilde{\Phi}_\alpha\rangle(\mathbf{r_r}, \mathbf{r_i})\right|^2, \tag{18}$$

$$E_{\text{var}}^2(\mathbf{r_r}) = \sum_\alpha^N F_\alpha(\mathbf{r_i}, \mathbf{r_r})^2 D_{\Phi,\alpha}(\mathbf{r_r}, \mathbf{r_i}), \tag{19}$$

with, following the derivation presented in Appendix A,

$$\langle\tilde{\Phi}\rangle = e^{-iD_0 - \frac{\sigma^2 K^2}{2}} L_x L_y \operatorname{sinc}\left(\frac{L_x A_0}{2}\right) \operatorname{sinc}\left(\frac{L_y B_0}{2}\right), \tag{20}$$

$$D_\Phi = e^{-\sigma^2 K^2} \sum_{m=1}^\infty \frac{(\sigma^2 K^2)^m}{m!} \frac{l^4}{m^2} \mathcal{F}_A(m)\mathcal{F}_B(m), \tag{21}$$

where

$$\mathcal{F}_A(m) = 1 - e^{-\frac{L_x^2 m}{l^2}}\cos(L_x A_0)$$
$$+ \sqrt{\pi}e^{-\frac{A_0^2 l^2}{4m}}\left[\operatorname{Re}\{A_m \operatorname{erfi}(A_m)\} - \operatorname{Re}\{A_m\}\operatorname{erfi}(\operatorname{Re}(A_m))\right], \tag{22}$$
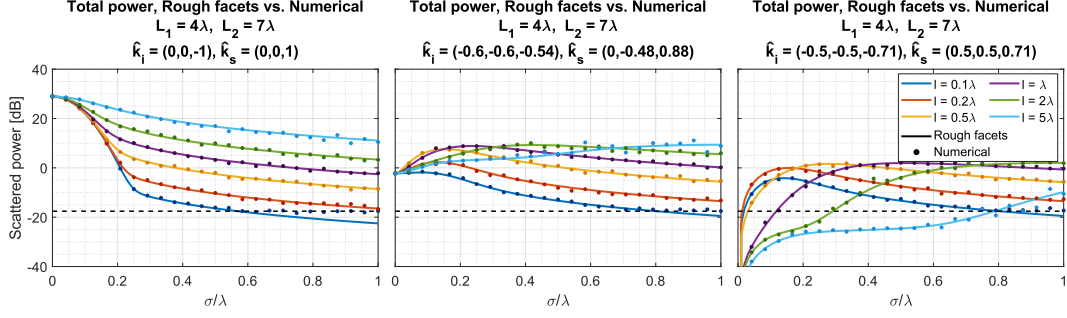
Figure 4: Numerical validation of (20) and (21) computed as total average power $\langle|\Phi|^2\rangle = |\langle\tilde\Phi\rangle|^2 + D_\Phi$ for different values of the surface RMS height, correlation length, and for different bistatic scattering directions (left: nadir backscatter; centre: arbitrary bistatic angles; right: off-nadir backscattering on non-principal axis). Solid lines: analytical values. Dots: numerical values computed over 100 trials. Black dashed line: numerical floor of the discretisation.

$$
\begin{aligned}
\mathcal{F}_B(m) = {} & 1 - e^{-\frac{L_y^2 m}{l^2}} \cos(L_y B_0) \\
& + \sqrt{\pi} e^{-\frac{B_0^2 l^2}{4m}} \left[\operatorname{Re}\{B_m \operatorname{erfi}(B_m)\} - \operatorname{Re}\{B_m\}\operatorname{erfi}(\operatorname{Re}\{B_m\}) \right],
\end{aligned}
\tag{23}
$$

and

$$
A_m = \frac{A_0 l^2 + i2L_x m}{2l\sqrt{m}}, \qquad B_m = \frac{B_0 l^2 + i2L_y m}{2l\sqrt{m}},
\tag{24}
$$

where A_0 and B_0 were defined in (5).

The coherent part of our formulation, equation (20), is nothing but the unperturbed phase response of a rectangle with an attenuation factor. The squared norm of this quantity appears when deriving the coherent backscattering law of a rough surface under the Kirchoff approximation (Kong, 2000). Similar and related formulae exist in other contexts [Carrer et al. (2019); Xu et al. (2021)], which is not surprising given that the rather immediate nature of its derivation. Regarding the incoherent part of our formulation, the much less trivial equation (21), it is the finite-surface equivalent of the incoherent backscattering law of a rough surface under the Kirchoff approximation (Kong, 2000). To our knowledge, (21) has thus not been derived before, and the novel contribution of our paper rests on the combined use of (20) and (21) for radar sounder applications. The latter formula's convergence or any choice of parameters is demonstrated in Appendix B. The differences and similarities between this formula and the infinite-terrain incoherent Kirchoff backscattering law found in (Kong, 2000; Tsang & Kong, 2004) is discussed in Appendix C.

To illustrate our formulation, we display in Figure 3 the magnitude in logarithmic scale of the coherent and incoherent parts of the phase response of an inclined facet, for three different cases of roughness. As the roughness is increased (top to bottom), we can see the coherent component (left) steadily decline, particularly in non-specular directions, as expected, whereas the incoherent component (right) takes over and becomes more isotropic, as expected. It is interesting to note that, for small to moderate amounts of roughness, the incoherent radiation pattern retains the memory of the shape of the facet, so that it is only at very high roughness level that the facet shape stops having an influence.

3.3 Reproduction of speckle from incoherent power

Formula (17) can be used to compute the coherent and incoherent power from a given DEM using the Stratton-Chu formula, using formulae (18) with (20), and (19) with (21), respectively. However, the resulting incoherent power is an *average* power, and although mathematically correct, it will not display any of the speckle behaviour seen in an actual radargram. This feature is nevertheless desirable for both visual fidelity and statistical accuracy of the simulated radargrams.

For this reason, we also propose an alternative way to simulate backscattering with the rough facet integrals, one where each incoherent return is assigned a random phase, in a way that generates the same average incoherent power (19).

Let a random phasor ϕ_r be defined as follows:

$$\phi_r \equiv \frac{\varepsilon_1 + i\varepsilon_2}{\sqrt{2}}, \text{ where } \varepsilon_1, \varepsilon_2 \sim \mathcal{N}(0, 1), \qquad (25)$$

$\mathcal{N}(0, 1)$ being the unit normal distribution. We define the coherent, incoherent, and total fields as follows:

$$E_{\text{coh}}(\mathbf{r_r}) = \sum_{\alpha}^{N} F_{\alpha}(\mathbf{r_i}, \mathbf{r_r}) \langle \tilde{\Phi}_{\alpha} \rangle (\mathbf{r_r}, \mathbf{r_i}), \qquad (26)$$

$$E_{\text{incoh}}(\mathbf{r_r}) = \sum_{\alpha}^{N} F_{\alpha}(\mathbf{r_i}, \mathbf{r_r}) \sqrt{D_{\Phi,\alpha}(\mathbf{r_r}, \mathbf{r_i})} \phi_r, \qquad (27)$$

$$E_{\text{tot}}(\mathbf{r_r}) = E_{\text{coh}}(\mathbf{r_r}) + E_{\text{incoh}}(\mathbf{r_r}). \qquad (28)$$

Effectively, we claim that when a random phase is drawn from distribution (25), the average power computed from the field (28) matches the average power obtained at (17). We demonstrate this equivalence in Appendix D. This effectively gives (28) Rician amplitude statistics, that is, a sum of a constant phasor and a complex Gaussian. We note that more complex formulations for speckle reproduction have been proposed [e.g. Haynes (2019)], but the relatively simple one we are using here produces amply satisfying results, as we will show in Sections 4.3 and 5.1.

In practice, formulation (17) will be more useful when coherent and incoherent power must be separated and when comparing with analytical solutions, whereas formulation (28) –which mixes coherent and incoherent fields beforehand– will be much more satisfying for simulations and forward-modelling. Additionally, the reproduction of speckle statistics from the scalar incoherent power is necessary if one wishes to apply any radargram analysis methods that relies on the power distribution of surface or clutter echoes on simulated radargrams (see Section 5.1.3).

4 Validation

We confirm the validity of our expressions (20) and (21) two ways. First, we perform a direct comparison of the analytical formulae against the statistics of the phase response of numerically-generated facets with Gaussian roughness (Section 4.1). Second, we incorporate the equations into a coherent large-facet Stratton-Chu simulator such as Gerekos et al. (2018), in which we conduct two experiments. The first is a comparison of the results of the proposed formulation with Haynes et al. (2018), an in-depth study of nadir power scattered from the first Fresnel zone under different roughness regimes (Section 4.2); the second takes a comprehensive sounding scenario over a terrain that is fractal at large scales, and compares the radar response (including off-nadir) over an oversampled DEM with a realisation of the roughness with that obtained over the original DEM with the rough facet integral (Section 4.3).

4.1 Rough facet integral in isolation

We start by validating formulae (20) and (21) independently of any simulator, by comparing them to the statistics of the phase contribution of isolated rectangular facets with realisations of Gaussian roughness. We assume the facet is in the XY plane. The domain of the finite facet is finely discretised and the complex surface phase integral is computed as a sum over the elements of the discretisation as

$$\Phi_{\text{num}} = (\Delta x)^2 \sum_j e^{i[k_{d,x}x_j + k_{d,y}y_j + k_{d,z}z(x_j,y_j)]}, \tag{29}$$

where $(k_{d,x}, k_{d,y}, k_{d,z})$ are the components of the wave vector difference, (x_j, y_j) are the coordinates of the discretised elements in the XY plane, $z(x_j, y_j)$ is the height of the random rough surface, and Δx is the side length of the square elements. The sum is taken over all points j that make up the facet, and the discretisation step is assumed to be the same in x and y.

Figure 4 compares the total average power $\langle |\Phi|^2 \rangle$ obtained analytically [*i.e.*, the sum of the coherent and incoherent components (20) and (21)] and numerically [*i.e.*, through equation (29) computed over many trials] as a function of the RMS roughness σ and surface correlation lengths l, using different combinations of incident and scattered directions. For more generality, the facet is taken to be a rectangle rather than a square. The facet size for the simulations is $L_1 = 4\lambda, L_2 = 7\lambda$. For each set of parameters, 100 realisations of a 2D Gaussian rough surface were generated and the phase integral computed. The generated surfaces are made 10 times larger than the largest correlation length, from which a facet of size $L_1 \times L_2$ is stamped; this ensures that there are enough correlation lengths in the generated surface for accurate surface statistics. The surfaces are discretised at $\Delta x = \lambda/40$. From Haynes et al. (2018), the numerical floor for this computation for low correlation lengths is $(\Delta x)^2 \mathcal{A}$ where $\mathcal{A} = L_1 L_2$ is the area of the facet and which is plotted as the dashed line. A value of $\lambda = 1$ was used in this test without loss of generality, as quantities involved are normalised by the wavelength.

The numerical and analytical results show excellent agreement in all cases. This was validated over a wide range of wave vector angles and facet sizes with the same results. These examples also show that even if the input parameters violate the Kirchhoff approximation (*i.e.*, correlation lengths, RMS roughness levels, or scattering angles that are too large) that the analytical equations accurately predict the literal evaluation of the statistical average powers of the scalar phase integral for Gaussian surfaces and isotropic Gaussian correlation function.

4.2 Nadir response: comparison with literature

The validity of (21) in isolation having been demonstrated, we now propose to validate the exactitude of a rudimentary radar simulator that includes the rough facet integral in the phase response of its facets.

In Haynes et al. (2018), the authors proposed a formula giving the coherent and incoherent power scattered at normal incidence from an rough disc that has the size of the first Fresnel zone. This disk has Gaussian roughness and has no large-scale topography.

4.2.1 Total power calculation

In our framework, this corresponds to a simulation where the DEM is a flat disk the size of the first Fresnel zone, where we neglect all the vectorial and reflectivity factors from the computation of the electric field. The Stratton-Chu formula we utilise is that for monostatic backscattering [*i.e.*, formula (9) with $\mathbf{r_r} = \mathbf{r_i}$].
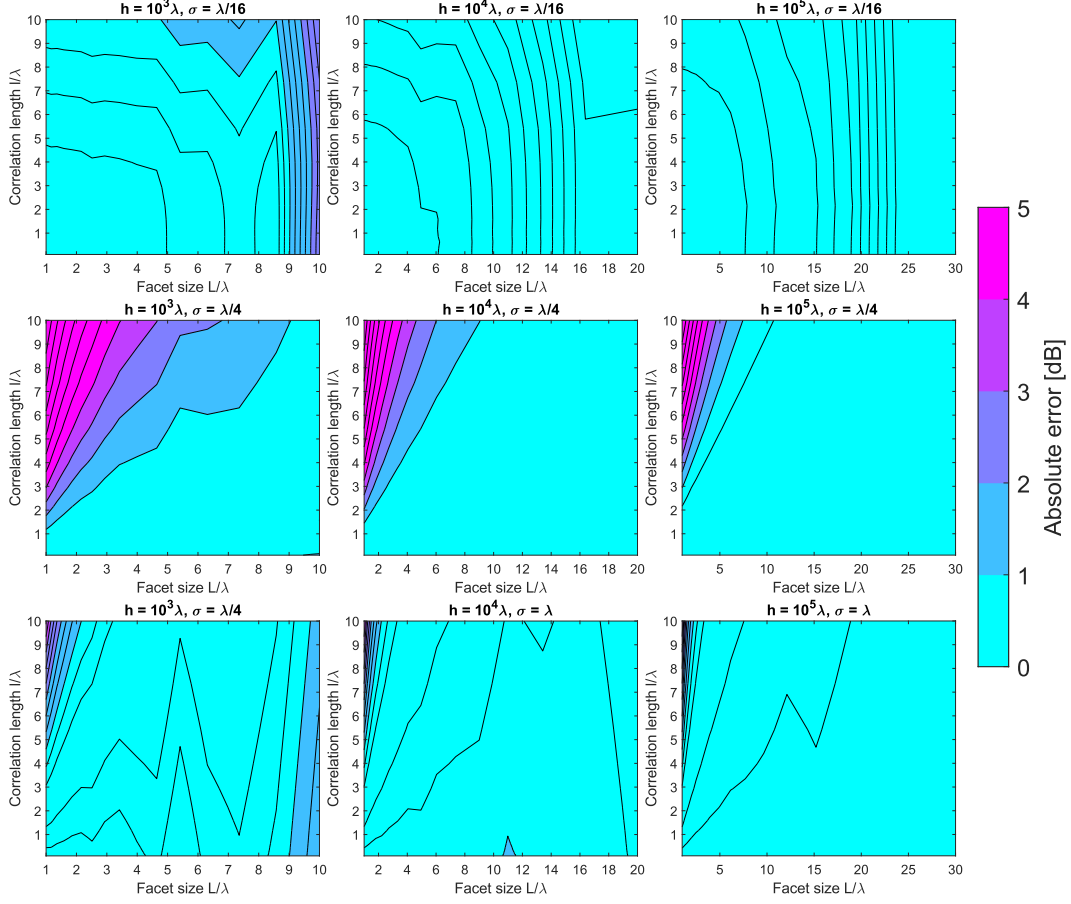
Figure 5: Comparison between the simulated backscattered power [sum of (33) and (34)] from the first Fresnel zone and the result from theory: λ-adimensionalised parametric scan in the (σ, l, L, h) space. 10 contour lines are shown in each plot.

Starting with a simplified emitting field

$$E_i(\mathbf{r}, \mathbf{t}) = \frac{V_i}{|\mathbf{r} - \mathbf{r_i}|} e^{ik_i|\mathbf{r}-\mathbf{r_i}|} s(t),\tag{30}$$

where $V_i = \sqrt{P_i}$ controls the amplitude of the emitter, taken here as the square root of the radiated power P_i so as to match the setup of Haynes et al. (2018). Neglecting reflection coefficients and vector-related quantities in the Stratton-Chu equation, we take

$$F_\alpha(\mathbf{r_i}, \mathbf{r_r}) = \frac{ik_i V_i}{(4\pi)^2 |\mathbf{r}_\alpha - \mathbf{r_i}|^2}\tag{31}$$

as the F factor in (12).

To leave processing out of the picture, we assume the emitted signal is a Gaussian pulse:

$$s(t) = \exp\left[-\pi \frac{B_w}{T_s}(t - t_0)^2\right],\tag{32}$$

where B_w is the instrument bandwidth, T_s the duration of the pulse, and t_0 the time of emission of the pulse.

We write that the simulated coherent and incoherent power can be expressed as:

$$P_{\text{coh}}(\mathbf{r_r}, t) = (4\pi)^2 \left[\sum_{\alpha}^{N} \frac{V_i s(t - \tau_\alpha)}{(4\pi)^2 |\mathbf{r}_\alpha - \mathbf{r_r}|^2} \langle \tilde{\Phi}_\alpha \rangle (\mathbf{r_r}, \mathbf{r_r}) \right]^2 , \tag{33}$$

$$P_{\text{incoh}}(\mathbf{r_r}, t) = (4\pi)^2 \sum_{\alpha}^{N} \left[\frac{V_i s(t - \tau_\alpha)}{(4\pi)^2 |\mathbf{r}_\alpha - \mathbf{r_r}|^2} \right]^2 D_{\Phi, \alpha}(\mathbf{r_r}, \mathbf{r_r}), \tag{34}$$

where τ_α represents the two-way travel time of electromagnetic waves from the radar to the facet α.

The total backscattered power is given by the sum of the coherent and incoherent powers as per (17).

4.2.2 Simulation setup

Using the equations above, we performed a systematic, λ-independent parametric scan over a range of one order of magnitude for the facet size L and two orders of magnitudes for the platform altitude h. We compare the obtained nadir power to the theoretical formulation for the power backscattered from a rough first Fresnel zone at nadir (Haynes et al., 2018).

In these simulations, we perform a hard cut-off at the first Fresnel zone boundary, and facets whose centres lie beyond this boundary are discarded. The most challenging aspect of this validation is thus the approximation of a disk with large square facets. For this reason, we must ensure the radar is properly centred on a facet of the flat DEM. Any other configuration will result in a lopsided footprint. This artificial requirement is only needed here, and has no effect when considering extended footprints, as in the next validation and applications.

4.2.3 Validation outcome

Figure 5 shows the result of this analysis. The cyan colour, which corresponds to an absolute error inferior to 1 dB, dominates the parameter scan. Looking at successive columns, we can see there is little effect of the altitude on the overall accuracy of our results. Looking at successive rows, we can see that the range of fidelity of the simulated response is the most constrained at the intermediate roughness of $\sigma = \lambda/4$. We will expand on the reasons for this in the following.

When the coherent term dominates (top row), the main limitation to accuracy is predictably the facet size. As the facets get larger, it becomes more and more difficult to correctly approximate the first Fresnel disk with squares, even with the linear phase approximation. These are essentially the limitations of Nouvel et al. (2004).

When the incoherent term starts to emerge (middle row), the simulator yields very accurate responses everwhere except where the correlation length of the small-scale roughness is larger than the facet itself. The reason for this is that, when the correlation length is larger than the facet size, the "roughness" that is being added to the facets corresponds to a shifting or a tilting of the entire facet rather than to a perturbation. With such facets, the roughness across the entire DEM no longer corresponds to that of the reference terrain in terms of correlation length (see also the discussion of Appendix Appendix C). We note that, this limination does not concern us from a practical point of view. Our goal is to incorporate the missing roughness scales from a poorly-resolved DEM where the facet height is considered correct, implying that, if there is small-scale roughness, its correlation length is must be comparable or smaller than the DEM resolution.

Table 1: Characteristics of the SHARAD, LRS , and MARSIS sounders as used throughout this paper, along with the resolution of the best available global DEM of their orbiting body, *i.e.*, the MOLA-HRSC blended DEM for Mars and the LOLA DEM for the Moon.

		SHARAD	LRS	MARSIS
Central frequency	[MHz]	20	5	1.3
Wavelength in vacuum	[m]	15	60	230
Bandwidth	[MHz]	10	2	1
Altitude	[km]	300	100	500
Sampling frequency	[MHz]	26.67	6.25	2.8
Chirp duration	[μs]	85	200	250
Transmitted power	[W]	10	800	5
PRF	[Hz]	700	20	127
Orbiting body		Mars	Moon	Mars
Best global DEM resolution	[m]	200	118	200

When the incoherent term dominates (bottom row), a similar remark can be made, although the limitation looks less strict. That is likely because at a high sigma, the excinction effect dominates over the specifics of the rough facet pattern.

In summary, the agreement between theory and our method is excellent, and deviates by no more than 1 dB in the vast majority of scientifically-relevant cases.

4.3 Full response in presence of topography: comparison with random realisations

After having successfully validated the simulator for a flat terrain and a footprint restricted to the first Fresnel zone, we conclude the validation with a maximally-comprehensive test. Starting from a DEM with large facets and long-range topography, and, considering the full radar response (nadir and off-nadir), we propose to compare the output of a Stratton-Chu simulator that includes the rough facet integral with that of a Stratton-Chu simulator ran on an oversampled DEM with a realisation of that small-scale roughness. Referring to Figure 1, we essentially compare the radargram obtained from the top DEM with the constant phase approximation, with the radargram obtained from the bottom DEM with the rough facet integral.

Due to the very high computational load of generating the simulations on the highly oversampled DEM, it is not realistic to perform a systematic analysis of the error, as we did in the case of nadir power (where the footprint is only as large as the first Fresnel zone). For this reason, we instead present three representative cases, corresponding to real-life sounders MARSIS (Jordan et al., 2009), LRS (Ono et al., 2010) and SHARAD (Croci et al., 2011), using facet sizes corresponding to that of the best global DEM of their corresponding planet (Fergason et al., 2018)(Smith et al., 2010). The characteristics of these radars are shown in Table 1.

4.3.1 Total power calculation

Unlike in the previous subsection, the complete Stratton-Chu formula (12) is used, and we are now taking into account the local Fresnel coefficients at the facets, as well

as the full vectorial and time-dependant aspects of the field. For this test, we make use of the formulation with speckle, so as to compare power histograms for clutter as well.

The time-domain signal $s(t)$ is a linear chirp, as with real instruments:

$$s(t) = \exp\left[i\pi \frac{B_w}{T_s}(t - t_0)^2\right], \tag{35}$$

where, as previously, B_w is the instrument bandwidth, T_s the duration of the pulse, and t_0 the time of emission of the pulse. When such a signal is used, a *range-compression* operation must be performed at the end to make features emerge. This consists of cross-correlating the received field with the reference signal.

Coherent and incoherent fields are computed as in (28), with added time-domain consideration discussed in Section 2.3. The fields are then projected onto the polarisation $\hat{\mathbf{e}}$ of the antenna, range-compressed, and converted into power. In summary, the total power is given by:

$$P(t, \mathbf{r_r}) = \frac{G\lambda^2}{4\pi} \left| \left\{ \sum_{\alpha}^{N} \left[\mathbf{F}_\alpha(\mathbf{r_r}, \mathbf{r_r}) \cdot \hat{\mathbf{e}}\right] \left[\langle\tilde{\Phi}_\alpha\rangle(\mathbf{r_r}, \mathbf{r_r}) + \right.\right.\right.$$
$$\left.\left.\left. \sqrt{D_{\Phi,\alpha}(\mathbf{r_r}, \mathbf{r_r})}\phi_r\right] s(t - \tau_\alpha) \right\} \otimes s(t) \right|^2, \tag{36}$$

where $G = 1.67$ is the gain of a dipole antenna and $\otimes$ represents a cross-correlation in the time-domain.

4.3.2 Simulation setup

For each sounder, four simulations are conducted. Two simulations with only long-range topography: one with large facets (LF) and one with small facets (SF); and two simulations with added small-scale roughness: one with large facets using the rough facet integral, and one with small facets using a realisation of the roughness on the DEM. We call "base" terrains those that only contain long-range topography.

The long-range topography is the same in all four cases, and modelled with fractional Brownian motion (fBm). The terrain has a dielectric constant of 5. The spacing between the acquisitions is taken to be 500 m in all cases. The small-facet "base" DEM is obtained by oversampling the original DEM to the desired resolution with linear interpolation. The small-facet rough DEM is obtain by adding the small-facet base DEM with a DEM that is a realisation of a Gaussian field with isotropic Gaussian correlation function with the desired σ and l. The small-facet DEMs have a resolution of $\lambda/10$, except for SHARAD, where computational limitations restricted us to $\lambda/5 = 3$ m.

We note that our rough integral formulations assume that small-scale roughness is perpendicular to the facet, for each considered facet, whereas our way of generating the rough SF DEMs is essentially equivalent to have the perturbation oriented along the z-axis. This might have non-negligible consequences, as we will see later.

The characteristics of the simulations are given in Table 2. For the LF base terrains, the parameter $0 < H < 1$ is the Hurst coefficient, and ζ is the RMS height difference at the scale of the resolution. We attempted to avoid any relationship between the roughness parameters and the L/λ ratio, generally the main driver of inaccuracy in simulations. This was possible for all parameters except the correlation length, which has an upper constraint given by the facet size in the rough integral, and a lower constraint given by the quality of the realisation in the SF DEM.

The small-scale roughness level used in these cases are relatively low, for two reasons. First, even a slight amount of roughness has a dramatic impact on off-nadir scattering, and we would like to illustrate this effect without drowning the nadir response,

Table 2: Summary of the terrain parameters used in the simulations of Section 4.3.

Radar	fBm topography (base)	Small-scale roughness
MARSIS	$H = 0.58, \zeta = 3.7\mathrm{m}$	$\sigma = \lambda/10, l = \lambda/3$
LRS	$H = 0.84, \zeta = 3.5\mathrm{m}$	$\sigma = \lambda/20, l = \lambda$
SHARAD	$H = 0.71, \zeta = 1.6\mathrm{m}$	$\sigma = \lambda/15, l = 6\lambda$

and second, small amounts of roughness are likely to be the preferred application domain of our method when used on real-life DEMs (see Section 5). We note that this does not necessarily makes these cases "easier", as the coherent component of the simulator is more sensitive than the incoherent one, and important small-scale roughness levels are actually easier to reproduce with the integrated simulator (see previous subsection).

4.3.3 Validation outcome

The resulting simulated radargrams are shown in Figure 6, which are arranged with the three instruments as columns, and the cases as rows. Visual comparison within each column of the first two radargrams (that is, the LF and the SF runs without small-scale roughness) shows the similarities and differences that can be expected between the linear phase approximation on large square facets –essentially the method of Nouvel et al. (2004)– and the constant phase approximation on small facets. Comparing the last two radargrams of each column (that is, the LF and SF runs that include small-scale roughness) highlights the contribution of the rough phase integral. Visual agreement between these rough runs is very good, except perhaps for the SHARAD simulation, where $L \approx 13.33\lambda$.

The analysis of these radargrams is shown in Figure 7-(left) in terms of average rangeline, and in Figure 7-(right) in terms of the clutter power histograms. In Figure 7-(left), the dotted curves are the average rangelines for the "base" terrain, for both large and small facets (blue and yellow curves, respectively). The solid curves represent the terrain with added small-scale roughness, either in the form of the rough phase integral or as a realisation on the SF DEM (red and purple curves, respectively). The "base" dotted curves are given for reference, whereas the small-scale roughness-related solid curves are the ones of interest. In Figure 7-(right), the histograms for the cases including small-scale roughness are plotted using the same colours.

The outcome of the MARSIS test, where $L \approx 0.87\lambda$ and $l = \lambda/3$, is excellent. Nadir power levels from the LF and SF simulations are in perfect agreement, whether small-scale roughness is added (solid curves) or not (dotted curves). Interestingly, off-nadir power is slightly overestimated in the "base" case, but is almost perfectly reproduced with large rough facets when small-scale roughness is considered in the $\lambda/10$ simulation. This mirrors results obtained in the previous subsections: when incoherent power dominates (as in the non-nadir regions of this test), results tend to be more accurate. We also remark that the jitter of the small-scale roughness curves is *not* structure: if the number of averaged rangelines would increase, the lines would get flatter and flatter. The power histograms of the LF and SF simulations involving small-scale roughness are also almost identical.

The LRS test, where $L \approx 2\lambda$ and $l = \lambda$, is also conclusive. A few discrepancies can nevertheless be noticed. Looking at the simulations that include small-scale roughness (solid curves), we observe an error of a few dB for the nadir power. Ignoring small-scale roughness (dotted curves), deviations start to appear is in the far off-nadir regime.
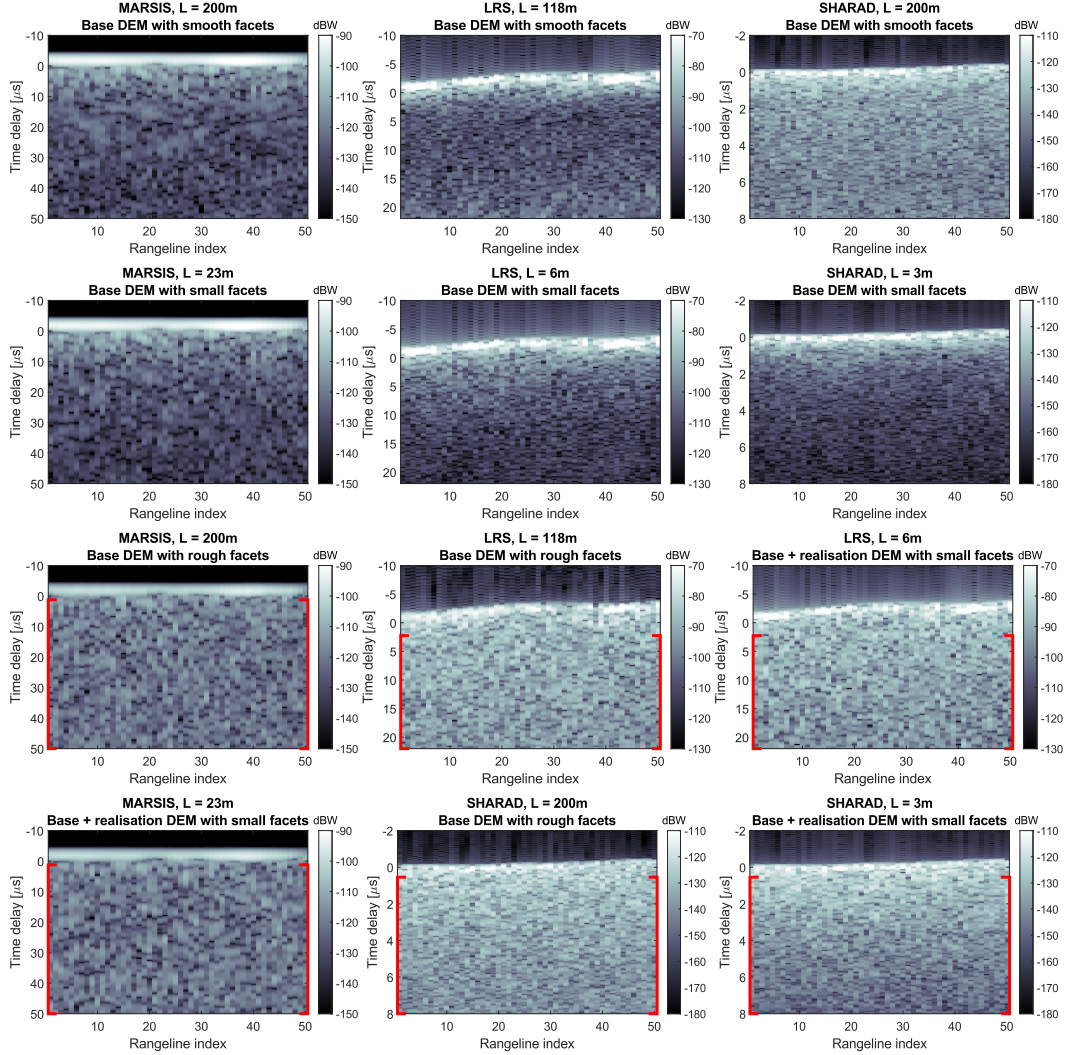
Figure 6: Comprehensive Stratton-Chu simulations [eq. (36)] using DEMs with long-range topography, with and without small scale roughness, for MARSIS (left), LRS (centre), and SHARAD (right). Results shown are using: the large-facet base DEM (top row), the oversampled base DEM (second row), the large facet base DEM using the rough phase integral (third row), and the oversampled base DEM where a random realisation of the considered small-scale roughness has been added to the DEM (bottom row). The parameters of the terrains are listed in Table 2. The average rangelines are shown for each case in Figure 7-(left). For the simulations involving small-scale roughness, the red boxes show the limits of the area for which the histograms shown in Figure 7-(right) were computed.
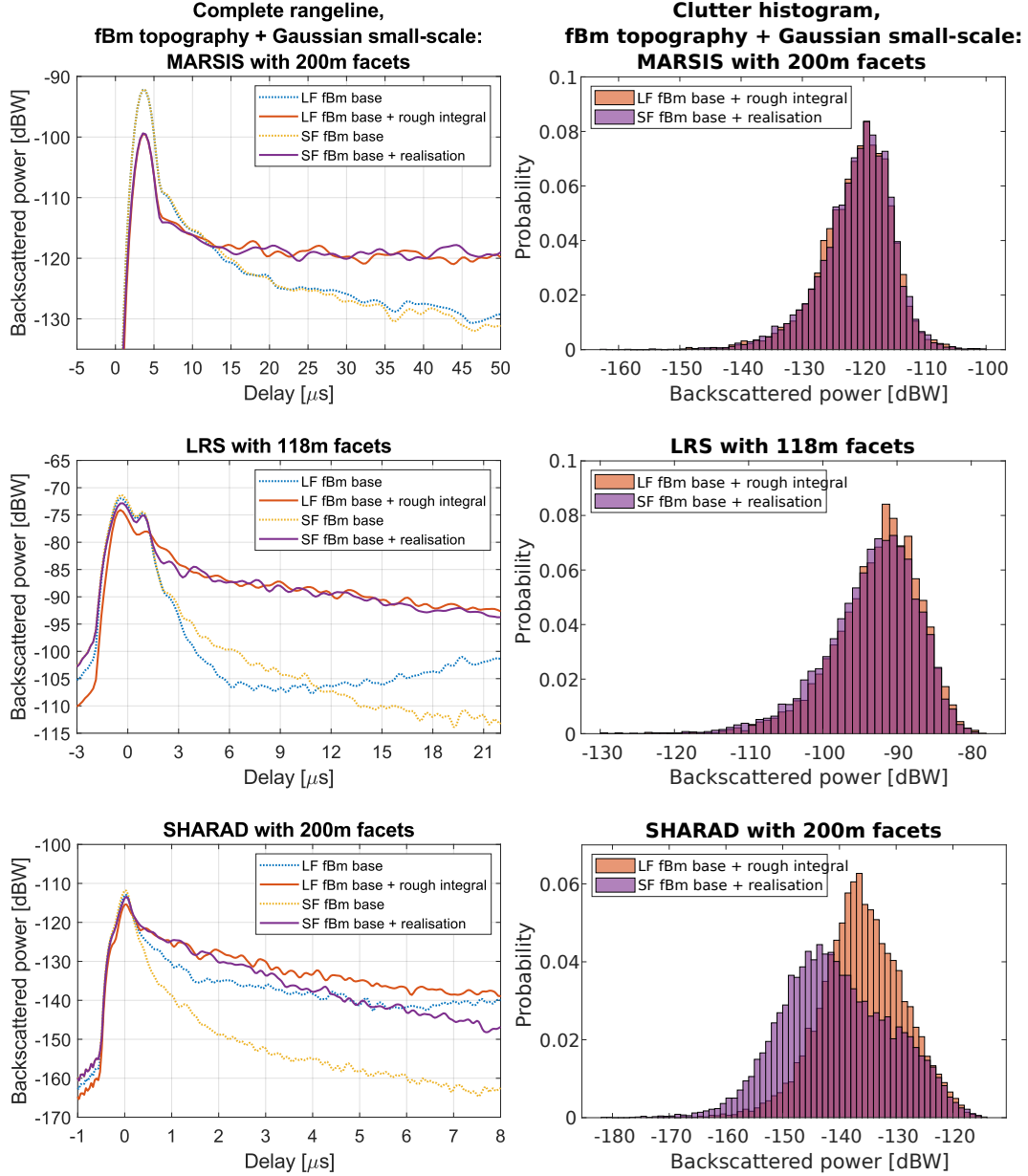
Figure 7: Average rangelines (left) and clutter histograms (right) of the radargrams shown in Figure 6: comparison between base terrain with large smooth facets (blue), base terrain with large rough facets (red), base terrain with small facets (yellow), and base terrain with small facets with an added realisation of the perturbation (purple). The parameters of the terrains are listed in Table 2.

When using triangular facets (not shown here), a much better agreement between the "base" LF and SF simulations was obtained. We thus believe the discrepancies are due to the limitations of the linear phase approximation on square facets, which are carried by both the smooth and rough simulations. In this case, it is worth noting the differences are still slight, and that the rough facet simulation is almost indistinguishable from the SF with a realisation of the roughness in terms of both clutter power angular dependence and clutter power histogram.

The SHARAD test, with $L \approx 13.33\lambda$, is the most challenging. The average range-line and histogram comparison highlights the visual discrepancy seen in Figure 6. Ignoring small-scale roughness (dotted curves), there is a slight discrepancy of a few dB for nadir power, and a difference in off-nadir power angle dependence can be observed. This issue is also carried to the simulations including small-scale roughness (solid curves). Essentially, the discrepancies observed in the LRS cases have all increased. In the presented test, we nevertheless remark that the agreement is excellent at time-delays of up to 3 μs, which corresponds to an apparent depth of 1.8 km. This should be satisfactory for most applications.

The main driver of differences between SF and LF simulations in the case of small-scale roughness seem to be L and l. There does not seem to be a correlation with σ, which is not surprising given the small σ involved. Due to the absence of satisfying analytical formulation for the backscattering from the type of terrains simulated here, and the computational load of simulating on the small-facet DEMs, it is difficult to envisage a way to disentangle the sources of errors in the (L, l, H, ζ) space, especially given the limitations on the range of possible l once L and λ are chosen. By reverting to scalar fields and Gaussian waveforms as in the previous section, the same discrepancies could be observed. We thus attribute them primarily to the limits of the linear phase approximation and the limitation of square facets in the case of large facets. The main issue with square facets, as noted in Berquin et al. (2015), is that they provide a discontinuous representation of the surface, leading to less accurate wavefront reconstruction. That is a problem that the use of triangular facets can partially solve (Berquin et al., 2015). The derivation of a rough facet integral for triangular facets, or indeed arbitrarily-shaped facets, is thus planned as future work. We also note that the use of small-facet simulations as reference should also be subject to caution, as we mention in point 4.3.2 of this subsection.

4.4 Discussion

We have first demonstrated that our formulae (20) and (21) are correct descriptions of a rough facet in isolation. The results of Figure 4 showed our formulae are able to accurately reproduce the scattering from a rough facet no matter the bistatic scattering angles we chose.

We have then characterised their range of validity when included in a basic electromagnetic simulator and considering the backscattering from a rough flat Fresnel disk, and we found the results to be accurate within less than 2 dB for most of the probed parameter space. The cases where the accuracy was lower was i) when the coherent component dominates (*i.e.*, low small-scale roughness), and ii) when the coherence length of the facet roughness was significantly larger than the dimensions of the facet. Limitation (i) is simply the consequence of the limitations of the linear phase approximation on square facets as described in Nouvel et al. (2004), whereas limitation (ii) refers to cases which do not have physical relevance in the real world.

Finally, considering a complete rangeline, the complete Stratton-Chu formula, and DEMs with significant topography, we compared the results of our simulator with the integrated rough facet formulation with those obtained from an oversampled DEM upon which small-scale roughness with the same characteristics was superimposed. In these tests, we have found that the method can safely be used with MARSIS and LRS on the
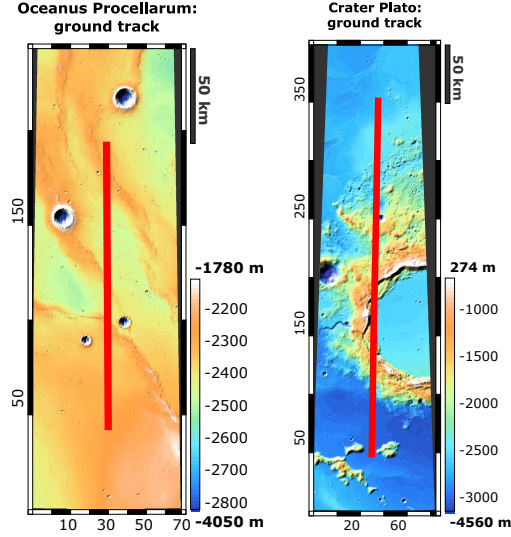
Figure 8: Ground tracks (red line) and DEMs (background) for the two radargrams presented in Section 5.1. Left: Oceanus Procellarum DEM, centred at (34.34°N, -61.12°E), and LRS track 20071223000958. Right: Crater Plato DEM, centred at (52.94°N, -11.70°E), and LRS track 20080821022958.

DEMs of their respective planet, and with correlation lengths that are of the order of the wavelength or smaller. However, the wide difference of facet length and wavelength in the case of SHARAD probably warrants some oversampling of the MOLA-HRSC DEM to ensure the off-nadir results are correct in any situation with the proposed formulation. We note that despite the limitations that were observed by thoroughly analysing the validation radargrams, visual comparisons of the LF and SF radargrams remains satisfactory in all cases, making the proposed simulator suitable for forward-modelling and clutter discrimination without such disclaimers.

5 Applications

To demonstrate the versatility and utility of our formulation, we develop two different contexts in which formulae (20) and (21) can be used. The first application is to better simulate radar echoes with a coherent Stratton-Chu simulator and coarsely-resolved DEMs. We demonstrate that the inclusion of rough facets with well-chosen small-scale roughness characterisations lead to much better reproduction of radargrams acquired by actual instruments. As a second application, we propose to use the coherent and incoherent radiation patterns we developed to better characterise subglacial water bodies based on their specular content, expanding on the work of Schroeder et al. (2014b).

5.1 Forward modelling with the proposed all-scale simulator

We show in this subsection simulated radargrams of natural terrains using the same comprehensive simulator described in Section 4.3 at equation (36), and we compare them to actual radargrams acquired over the same terrain. We chose to reproduce lunar radargrams acquired by the LRS instrument. The reasons for this choice are several: (i) the SNR of the range-compressed data product is high, thus we do not have to resort to radargrams that have undergone advanced SAR processing, (ii) the global DEM of the Moon has a good resolution compared to the LRS instrument ($L \approx 2\lambda$), and we verified in Section 4.3 that it the errors of the LPA/square facets are low for this case, and (iii) the
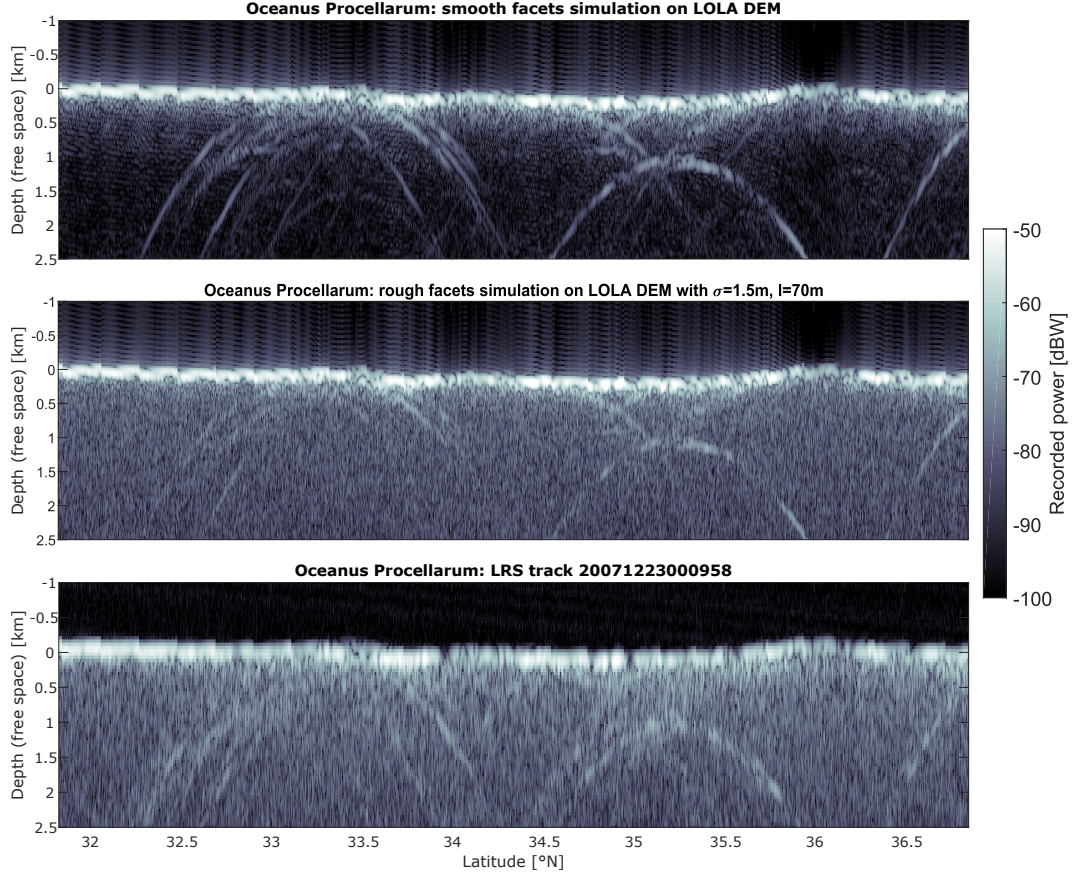
Figure 9: Illustration of the effect of rough facets in a Stratton-Chu simulation of a real radargram of Oceanus Procellarum, Moon. Top: simulation of LRS track 20071223000958 using the LOLA DEM and smooth facets. Middle: simulation of LRS track 20071223000958 using the LOLA DEM and rough facets (this paper). Bottom: original LRS radargram 20071223000958.

Moon has no ionosphere, removing the need for ionosphere distortions correction measures.

Two areas were picked to illustrate the capabilities of the Stratton-Chu simulator combined with the proposed rough facet formulation: a portion of eastern Oceanus Procellarum captured in LRS track 20071223000958, which represents a smooth area, and a limb of Crater Plato captured in LRS track 20080821022958, which represents a clutter-dominated area. The ground track of these two radargrams is shown in Figure 8. These tracks correspond to the tracks of the simulated radargrams over the Lunar Orbiter Laser Altimeter (LOLA) DEMs (Smith et al., 2010), locally re-projected in orthographic projection in each case.

The dielectric constant of the surface was assumed to be uniformly equal to 4 (Ono et al., 2009). In order to factor out any uncertainty on absolute emitted power, processing, and surface reflectivities, we opted for a normalisation of our simulated radargrams by an amount that is constant for both terrains. This constant was computed from the smoothest areas of the Oceanus Procellarum radargram (first 100 rangelines); since lunar maria are the Moon's smoother surfaces, this is the straightforward choice to measure non-roughness-related differences of power. We compared the average rangeline in the rough facet simulation with that of the LRS track. The normalisation constant we extracted is 18.1 dB. This amount is added to all LRS simulations, smooth or rough, included in this section. A hamming-windowed chirp was used, as in the LRS instrument, to model the time-domain signal as accurately as possible.

5.1.1 Oceanus Procellarum

The rough-facet simulation was produced with a facet-level roughness of $\sigma = 1.5$ m and $l = 70$ m, which is consistent with the decametre-scale roughness of lunar maria (Cai & Fa, 2020). The comparison between the smooth-facet simulation, the rough-facet simulation, and the original radargram can be seen in Figure 9.

The gain in fidelity of the diffuse clutter rendition in the rough facet simulation is dramatic, and illustrates how even gentle amounts of roughness have a significant impact in off-nadir scattering. The appearance of specular clutter is also improved, as the rough-facet simulation no longer shows range-migration hyperbolae that are not present in the original picture.

Subtle differences between the rough-facet simulation and the original radargram in the near-surface regime can be observed, in particular at latitudes larger than 35°N. These can be due to slight local variations of surface properties (*e.g.*, roughness, dielectric constant), or can be indicative of subsurface scattering (*e.g.*, volumetric effects or layering). By factoring out the effects due to small-scale roughness with given characteristics, this example highlights how forward-modelling can be used for hypothesis-testing.

5.1.2 Crater Plato

We chose $\sigma = 1.9$ m and $l = 80$ m for the rough-facet simulation of Crater Plato, modelling a roughness that sits between that of lunar maria and that of lunar highlands (Cai & Fa, 2020), which we believe is realistic for a crater sitting between two maria. The comparison between the smooth-facet, rough-facet, and original radargrams can be seen in Figure 10. In the simulated radargrams, an artefact can be observed at a depth of about 4 km. This corresponds to a Bragg resonance from the regular lattice that characterises the DEM (Nouvel et al., 2004)[1].

---

[1] If needed, the position and strength of these artefacts can be reduced to acceptable levels through a resampling of the DEM.
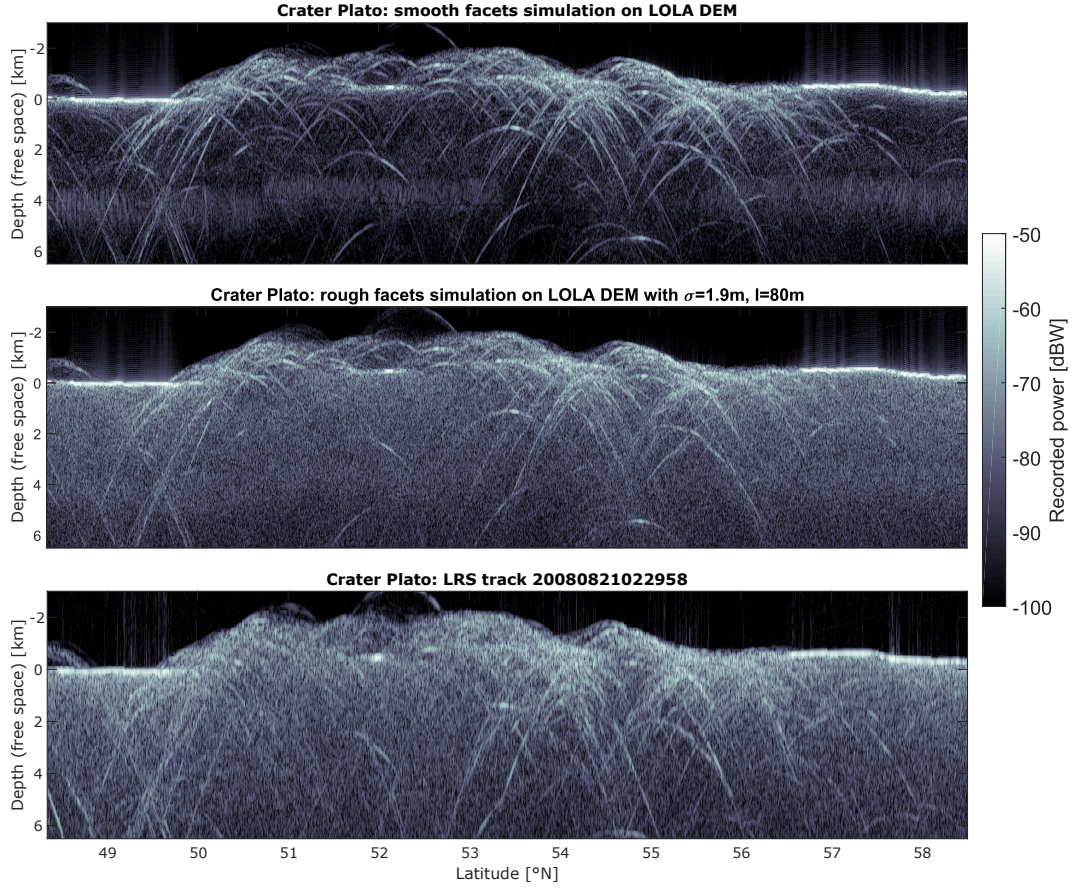
Figure 10: Illustration of the effect of rough facets in a Stratton-Chu simulation of a real radargram of Crater Plato, Moon. Top: simulation of LRS track 20080821022958 using the LOLA DEM and smooth facets. Middle: simulation of LRS track 20080821022958 using the LOLA DEM and rough facets (this paper). Bottom: original LRS radargram 20080821022958.

Similar comments can be made for this case regarding the aspect of diffuse and specular clutter, adding credence to the fact the rough-facet simulator can also be applied to areas with rich topography. Also of notice are the areas where the original radargram displays less diffuse clutter, *e.g.*, around latitudes of 54°N and 55.3°N, a feature which is also visible in the simulation.

5.1.3 Perspectives

One important aspect is that inclusion of roughness at facet level solves the long-standing problem of clutter simulators displaying too much specular clutter (Berquin et al., 2015; Gerekos et al., 2018). Ridden of an overabundance of parasitic clutter, the proposed method is thus expected to be helpful for geological interpretation of radargrams. Due to our formulation being closed-form, a Stratton-Chu simulator of surface backscattering fitted with the proposed rough phase integral uses similar computational resources as a simulator fitted with the regular linear phase approximation, thus being very competitive with respect to finite-element methods [see e.g. Gerekos et al. (2018)].

As σ and l affect the off-nadir angle-dependence of backscattered power in different ways, it is reasonable to assume that the parameter space could be constrained univoquely for a given radargram. The proposed simulator could thus be used within an iterator to extract the small-scale roughness of a given terrain. We defer the construction of a proper inversion algorithm to a future study. Such a method would complement other roughness-estimation methods such as reflectometry (Grima, Blankenship, et al., 2014; Grima, Schroeder, et al., 2014).

Lastly, we note that facet-level roughness is likely better described with self-affine description (Landais et al., 2015). However, given the relatively constrained area that is covered by a typical DEM facet, the scale-dependence of roughness is likely to be less relevant at scales that affect radar backscattering. This is a probable reason why we are able to reproduce natural radargrams with rather high fidelity using a Gaussian distribution of heights with an isotropic Gaussian correlation function. For the same reason, more complicated roughness models such as fractional Brownian motion (fBm) could prove necessary if we are dealing with DEMs with resolutions of the order of the kilometre. In this case, we could envision adapting fBm scattering laws (Iodice et al., 2012) to the facet method to solve this problem.

5.2 A subsurface application: estimating subglacial water geometry

In Schroeder et al. (2014a), the authors treated the case of flat, specular, bright, coherent, anisotropic subglacial water bodies observed beneath Thwaites Glacier, West Antarctica using airborne radar sounding data. In this paper, the authors exploited the fact that the water bodies were coherent, flat, specular, and bright to assume that the variation in post-focusing bed echo power as a function of SAR focusing aperture was determined by the scattering function of the subglacial water bodies alone. The authors describe this scattering function of the basal ice-water interface in terms of the "specularity content" S_c of the echo given by $S_c = S(S + D)^{-1}$, where S is the "specular" component of echo and D is the "diffuse". In Schroeder et al. (2014a), these components are estimated by focusing the radar sounder data with SAR focusing apertures spanning different ranges of angles θ at the ice-bed interface. By focusing with two different apertures, the authors could estimate the aperture-independent contribution of S and the aperture-dependent contribution of D to the focused echo power.

The authors further exploited the anisotropy of the specularity content of the observed drainage-aligned high-specularity portion of the upper Thwaites Glacier catchment (Schroeder et al., 2013) to assume that the reflecting geometry of the subglacial water bodies could be approximated by the radar cross-section of a rectangular plate.
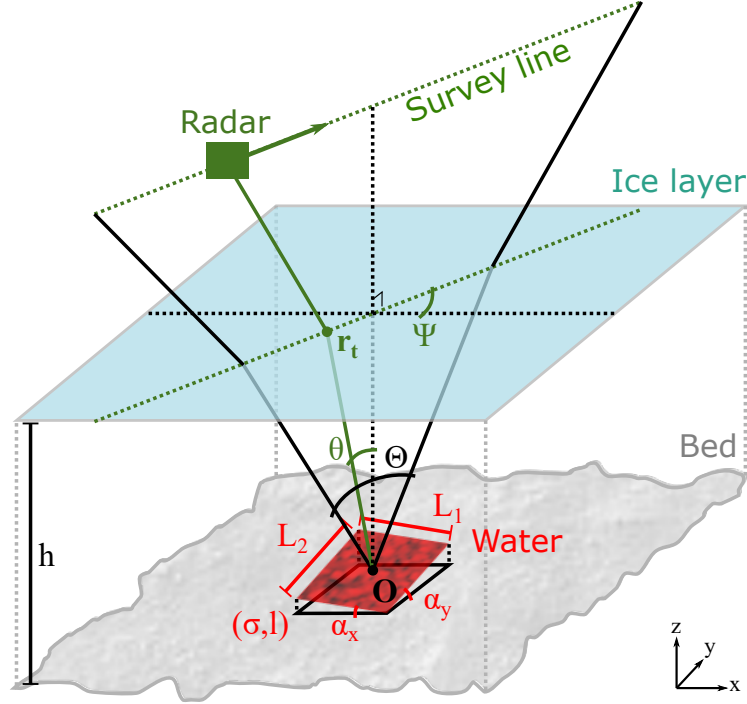
Figure 11: Geometry of the problem treated in Section 5.2, that is, the application of our rough facet formulae to the characterisation of small subglacial water bodies. The water body is modelled as a single rough facet.

The authors then integrated the scattering function that plate across θ to illustrate the dependence of S_c on water body of length L_1, width L_2, and survey orientation Ψ (Schroeder et al., 2014a). These quantities are shown in Figure 11. Both this calculation and the definition of S_c itself in Schroeder et al. (2014a) implicitly assume that non-coherent contributions to the scattering function of basal water bodies and SAR-focused bed echo power are negligible. However, our own results show that even quasi-specular interfaces can have significant incoherent components to the angular-dependence of their scattering functions.

The single-facet scattering functions presented in this paper provide expressions for both the coherent and incoherent contributions to the scattering function of a single, flat, rectangular facet with wavelength-scale or subwavelength-scale roughness. Therefore, our results can provide improved constraints on the geometry of subglacial water bodies that meet the same simplifying assumptions as those addressed in Schroeder et al. (2014a). The most significant of these assumptions is that the bed echo power returned from the water body dominates any power from off-nadir clutter (so that the latter can be neglected in our single-facet simulation).

We can thus generalise the model of Schroeder et al. (2014a) as follows. First, we may do away with the need for two different apertures and subsequent the separation of "specular" and "diffuse" distinctions, and instead compute the total integrated power as a function of the aperture angle. This gives a presumably unique curve for the set of parameters that describe the facet and the observation, which can be used for parameter inversion. Second, our formulation also allows the water body to have a slope in the x and y directions, shown as α_x and α_y, respectively. Third, we are able to include both the RMS height and the correlation length of such a rough body, under the usual assump-
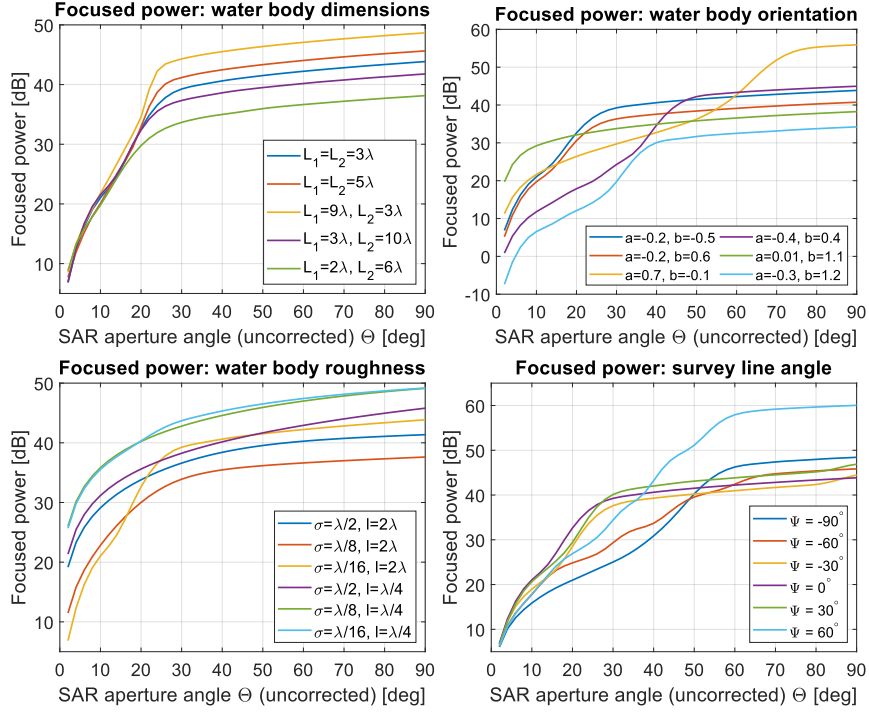
Figure 12: Characteristic focused power curves as a function of the uncorrected SAR aperture angle [formula (37)] of a water body with the following default properties: roughness $\sigma = \lambda/16, l = 2\lambda$, plane equation [formula (3)] with $a = -0.2, b = -0.5$, dimensions $L_1 = L_2 = 3\lambda$, survey line angle $\Psi = 0°$. These four properties are varied in isolation in each plot.

tion of a Gaussian distribution of heights and isotropic Gaussian correlation function, which we denote with the usual σ and l symbols.

In particular, equations (20) and (21) must both be integrated across the angles spanned by the SAR focusing window, and then scaled by the relevant processing gain (with the coherent power increasing proportional to the processing gain and the incoherent power increasing like its square root) before summation (Raney, 2011). The total power as a function of the integration angle Θ can thus be written as

$$P_{\text{foc}}(\Theta) \sim \int_{-\Theta/2}^{\Theta/2} N_{\text{acq}} \left| \langle \tilde{\Phi} \rangle (\mathbf{r_t}, \mathbf{r_t}) \right|^2 + \sqrt{N_{\text{acq}}} D_{\Phi}(\mathbf{r_t}, \mathbf{r_t}) d\theta, \tag{37}$$

where N_{acq} is the number of acquisitions within the span defined by Θ and $\mathbf{r_t}$ is the position on the surface shown in Figure 11 and is a function of θ:

$$\mathbf{r_t} = (h \tan\theta \cos\Psi, h \tan\theta \sin\Psi, h), \tag{38}$$

assuming without loss of generality that the origin $\mathbf{O}$ coincides with the water body centre. The angle to the radar can be computed from Snell's law, but this calculation will be ignored in this exercise. We therefore refer to Θ as the uncorrected SAR aperture angle.

In Figure 12 we show a few examples of these characteristic focused power curves, and how they vary as we modify various properties of the water body. As with the previous application (Section 5.1), we defer the definition of an inversion method and the characterisation of its precision to a later paper, but the presented curves illustrate how

this method can be used to "fingerprint" subglacial water bodies. We assume the acquisitions are evenly spaced in θ, with a spacing of $1°$, and derive the number of acquisitions accordingly. In reality the acquisitions are equidistant, but this approximation is acceptable for illustrative purposes. The subsurface index of refraction, which affects the wavenumber k, was taken to be $n_{ice} = \sqrt{3}$.

The method presented in Schroeder et al. (2014a) can therefore be considered a particular case of choosing two apertures Θ_1 and Θ_2 along this characteristic curve.

Even at the single-facet level, this treatment allows for more precise constraints on the geometry of flat subglacial water bodies which can be approximated as rectangles (Schroeder et al., 2014a). The generality of the formulation also allows the straightforward extension of the specularity concept to include the full range of aperture lengths which can provide even stronger empirical constraints on the full scattering function of the water body including its roughness [e.g. from accreted ice as in MacGregor et al. (2009)] and its slope, [e.g. Castelletti et al. (2019); Ferro (2019); Heister and Scheiber (2018); Oswald and Gogineni (2008)]. Once the model is extended to realistic target geometries spanning more than a single facet, the approach can treat the full range of subglacial water body geometries and sizes (MacKie et al., 2020) including those with patches much larger than $\mathcal{O}(\lambda)$.

6 Conclusions

We have derived expressions for the phase contribution of a rough, arbitrarily-inclined, rectangular facet under the linear phase approximation, assuming a zero-mean Gaussian distribution of height with an isotropic Gaussian correlation function. The resulting phase integral naturally splits into a coherent and an incoherent term. We have extensively validated the obtained formulae, both in isolation and within Stratton-Chu simulators, constrained their domain of application as much as technically possible, and concluded the formula can be used without risks for facet lengths and correlation lengths of the order of a few wavelengths, regardless of the facet RMS height.

We demonstrated how the facet incoherent power could be used to accurately model speckle within a Stratton-Chu simulator, and applied these results to simulations of LRS radargrams over diverse types of terrains. The results showed how inclusion of the rough facet formalism significantly enhances the fidelity of simulations, even with subtle amounts of facet-level roughness. Additionally, we have shown that the problem of characterising the radar signature of small subglacial water bodies is well-suited for the proposed model. By modelling these water bodies as a single rough rectangular facet, we showed how our formalism improves on state-of-the-art methods by removing the need for assumptions on the geometry of these bodies and the nature of their backscattered signals.

For a given wavelength, the accuracy of our formulation is mainly limited by two factors, which are the facet size and the correlation length. Considering the best global DEMs of the Moon and of Mars, we showed that the proposed method can satisfactorily simulate LRS and MARSIS radargrams with rough facets, but that in the case of SHARAD, some oversampling of the MOLA-HRSC DEM of Mars is probably advised.

Future work is envisioned to be as follows. First, the computations shown here will be generalised to other facet shapes, with triangular facets being the polygon of most interest. Triangles provide a much better medium for the facetisation of DEMs, and a rough triangular facet phase integral would provide a true generalisation of Gerekos et al. (2019) and Gerekos et al. (2018). This would open the way to more accurate multilayer Stratton-Chu descriptions, with numerous applications for terrestrial or planetary radar science. We could also consider generalising this model to other types of roughness.

7 Acknowledgements

8 Open Research

The codes used in this paper were written in MATLAB. The rough-facet Stratton-Chu cluttergram simulator used in this work is based on Gerekos et al. (2018), and its source code is available at `http://doi.org/10.5281/zenodo.7051503`. The lunar LRO LOLA DEMs were created through the UGSG Imagery Processing Cloud, and the source files are available at `http://pds-geosciences.wustl.edu/missions/lro/lola.htm`. The scripts used for fBm and Gaussian surface generation are available on MATLAB File Exchange (Botev, 2016, 2022). Finally, the LRS data is available at `http://darts.isas .jaxa.jp/planet/pdap/selene/`.

Appendix A Derivation of $\langle \tilde{\Phi} \rangle$ and D_Φ

This derivation picks up from equation (17) in the body of the text. We start by injecting the perturbed phase (14) into the facet phase integral (2):

$$\tilde{\Phi} = \oiint_A \phi(\mathbf{r_i}, \mathbf{r_r}, \mathbf{r}') e^{-iK\delta(\mathbf{r}')} d\mathbf{r}'. \tag{A1}$$

Using the fact that the stochastic and deterministic parts of (A1) are separable, the expressions for the ensemble-averaged phase response $\langle \tilde{\Phi} \rangle$ and its square norm $\langle |\tilde{\Phi}|^2 \rangle = \langle \tilde{\Phi}\tilde{\Phi}^\dagger \rangle$ can be easily derived. Using basic properties of the log-normal distribution, we obtain

$$\langle \tilde{\Phi} \rangle = \oiint_A \phi(\mathbf{r}') \langle e^{-iK\delta(\mathbf{r}')} \rangle d\mathbf{r}' = \Phi e^{-\sigma^2 K^2/2}, \tag{A2}$$

$$\langle |\tilde{\Phi}|^2 \rangle = \oiint_A d\mathbf{r}' \oiint_A d\mathbf{r}'' \phi(\mathbf{r}')\phi(\mathbf{r}'')^\dagger \langle e^{-iK[\delta(\mathbf{r}')-\delta(\mathbf{r}'')]} \rangle, \tag{A3}$$

$$= \oiint_A d\mathbf{r}' \oiint_A d\mathbf{r}'' e^{i\mathbf{k_d}\cdot(\mathbf{r}'-\mathbf{r}'')} e^{-\sigma^2 K^2[1-C(|\mathbf{r}'-\mathbf{r}''|)]}, \tag{A4}$$

where we dropped the $\mathbf{r_i}, \mathbf{r_r}$ dependencies for clarity. Equation (A2) yields formula (20).

In the linear phase approximation, we have

$$\mathbf{k_d} \cdot (\mathbf{r}' - \mathbf{r}'') = A_0(x' - x'') + B_0(y' - y''). \tag{A5}$$

From the decomposition (17), we see that the Φ-dependent terms of E_{var} will take on the form of an average of the intensity minus the intensity of the average. We denote

$$D_\Phi \equiv \langle |\tilde{\Phi}|^2 \rangle - |\langle \tilde{\Phi} \rangle|^2 = \oiint_A d\mathbf{r}' \oiint_A d\mathbf{r}'' e^{i\mathbf{k_d}\cdot(\mathbf{r}'-\mathbf{r}'')} \left(e^{-\sigma^2 K^2[1-C(|\mathbf{r}'-\mathbf{r}''|)]} - e^{-\sigma^2 K^2} \right), \tag{A6}$$

the phase contribution of the fluctuating part of the intensity. It is equal to

$$\begin{aligned} D_\Phi = \int_{-L_x/2}^{L_x/2} dx' \int_{-L_x/2}^{L_x/2} dx'' \int_{-L_y/2}^{L_y/2} dy' \int_{-L_y/2}^{L_y/2} dy'' e^{i[A_0(x'-x'')+B_0(y'-y'')]} \\ \cdot \left(e^{-\sigma^2 K^2 \left[1-C\left(\sqrt{(x'-x'')^2+(y'-y'')^2}\right)\right]} - e^{-\sigma^2 K^2} \right), \end{aligned} \tag{A7}$$

where L_x and L_y were defined in (8). This integral is usually solved through the usual centre-difference change of variable with unit Jacobian $\mathbf{u} \equiv \mathbf{r}' - \mathbf{r}''$, $\mathbf{v} \equiv (\mathbf{r}' + \mathbf{r}'')/2$. With the linearisation (A5), we obtain:

$$D_\Phi = \int_{-L_x}^{L_x} du_1 \int_{-L_y}^{L_y} du_2 (L_x - |u_1|)(L_y - |u_2|) e^{i(A_0 u_1 + B_0 u_2)} \left(e^{-\sigma^2 K^2 [1 - C(|\mathbf{u}|)]} - e^{-\sigma^2 K^2} \right).$$

$$\text{(A8)}$$

The exponentials relating to the perturbation can be expanded as a Taylor series as $e^{\sigma^2 K^2 C(|\mathbf{u}|)} = \sum_{m=0}^{\infty} (\sigma^2 K^2)^m C^m(|\mathbf{u}|)/m!$. We furthermore assume that the perturbation is characterised by an isotropic Gaussian correlation function

$$C(|\mathbf{u}|) = e^{-|\mathbf{u}|^2/l^2}, \tag{A9}$$

where l is the correlation length. Thus, by factorising $e^{-\sigma^2 K^2}$, we obtain (Kong, 2000) $e^{-\sigma^2 K^2 [1 - C(|\mathbf{u}|)]} - e^{-\sigma^2 K^2} = e^{-\sigma^2 K^2} \sum_{m=1}^{\infty} (\sigma^2 K^2)^m e^{-m|\mathbf{u}|^2/l^2}/m!$. Inserting this into (A8), the integral involves only the linearised phase along with an exponential of $u_1^2 + u_2^2$. We obtain that D_Φ can be decomposed into four integrals:

$$D_\Phi = e^{-\sigma^2 K^2} \sum_{m=1}^{\infty} \frac{(\sigma^2 K^2)^m}{m!} (I_1 + I_2 + I_3 + I_4), \tag{A10}$$

where

$$
\begin{aligned}
I_1 &= \int_0^{L_x} du_1 \int_0^{L_y} du_2 (L_x - u_1)(L_y - u_2) \phi_\epsilon, \\
I_2 &= \int_{-L_x}^0 du_1 \int_{-L_y}^0 du_2 (L_x + u_1)(L_y + u_2) \phi_\epsilon, \\
I_3 &= \int_0^{L_x} du_1 \int_{-L_y}^0 du_2 (L_x - u_1)(L_y + u_2) \phi_\epsilon, \\
I_4 &= \int_{-L_x}^0 du_1 \int_0^{L_y} du_2 (L_x + u_1)(L_y - u_2) \phi_\epsilon,
\end{aligned}
\tag{A11}
$$

and $\phi_\epsilon \equiv e^{i(A_0 u_1 + B_0 u_2) - m(u_1^2 + u_2^2)/l^2}$.

From here, since the bounds of the double integrals are independent of each other, the primitives that appear in (A11) can ultimately be reduced to these two identities:

$$\int e^{iax - bx^2} dx = -i \frac{e^{-\frac{a^2}{4b}}}{2} \sqrt{\frac{\pi}{b}} \mathcal{E}(x), \tag{A12}$$

$$\int x e^{iax - bx^2} dx = -\frac{e^{iax - bx^2}}{2b} + \frac{a e^{-\frac{a^2}{4b}} \sqrt{\pi}}{2\sqrt{b^3}} \mathcal{E}(x), \tag{A13}$$

where a and $b > 0$ are real factors, and where we used the shorthand notation

$$\mathcal{E}(x) \equiv \text{erfi}\left(\frac{a}{2\sqrt{b}} + i\sqrt{b} x \right), \tag{A14}$$

where $\text{erfi}(z) \equiv -i \, \text{erf}(iz)$ is the imaginary error function, and $\text{erf}(z) \equiv (2/\sqrt{\pi}) \int_0^z e^{-t^2} dt$ is the error function (Abramowitz & Stegun, 1964; Weisstein, 2022). The first identity can be obtained from the definition of the error function, by completing the square in the exponential argument and carrying out the appropriate change of variables. The second integral can be obtained from the first through integration by parts, and by using fundamental properties of the error function (Weisstein, 2022).

Using these two results along with purely algebraic manipulations, formula (A10) can be re-expressed into (21). In particular, the $\text{Re}\{\cdot\}$ operators appear naturally within this process using $\text{erfi}(z^\dagger) = [\text{erfi}(z)]^\dagger$.

Appendix B Convergence analysis

We gather under the quantity $D_{\Phi,m}$ all the elements that are being summed in (21):

$$D_\Phi = e^{-\sigma^2 K^2} \sum_{m=1}^{\infty} D_{\Phi,m}. \tag{B1}$$

We will demonstrate the (absolute) convergence of this series.

A lot of different positive constants are involved in the $D_{\Phi,m}$ terms. We chose a real constant $C > 0$, supposedly larger than any combination of m-independent factors found in $D_{\Phi,m}$, so that we can write

$$|D_{\Phi,m}| \leq \frac{C^{2m}}{m!m^2}[1 + Ce^{-Cm} + Ce^{-C/m}S_m]^2, \tag{B2}$$

where

$$S_m \equiv |\operatorname{Re}\{C_m \operatorname{erfi}(C_m)\}| + |\operatorname{Re}\{C_m\}\operatorname{erfi}(\operatorname{Re}\{C_m\})|, \tag{B3}$$

and

$$C_m \equiv \frac{C_1}{\sqrt{m}} + iC_2\sqrt{m}, \tag{B4}$$

where C_1 and C_2 are real positive constants taken such that S_m is greater or equal than both $\operatorname{Re}\{A_m \operatorname{erfi}(A_m)\} - \operatorname{Re}\{A_m\}\operatorname{erfi}(\operatorname{Re}\{A_m\})$ and $\operatorname{Re}\{B_m \operatorname{erfi}(B_m)\} - \operatorname{Re}\{B_m\}\operatorname{erfi}(\operatorname{Re}\{B_m\})$. Notice that all the terms are positive in the right-hand side of (B2), unlike in $D_{\Phi,m}$, in order to ensure the inequality is always true.

The right-hand side of (B2) can be expanded in a sum of six terms:

$$|D_{\Phi,m}| \leq \frac{C^{2m}}{m^2m!} + \frac{C^{2+2m}e^{-2Cm}}{m^2m!} + \frac{C^{1+2m}e^{-Cm}}{m^2m!}$$
$$+ \frac{2C^{1+2m}e^{-C/m}S_m}{m^2m!} + \frac{2C^{2+2m}e^{-C(1/m+m)}S_m}{m^2m!} + \frac{C^{2+2m}e^{-2C/m}S_m^2}{m^2m!}, \tag{B5}$$
$$\equiv d_1 + d_2 + d_3 + d_4 + d_5 + d_6. \tag{B6}$$

We will examine the absolute convergence of their series through the d'Alembert criterion[2]. It can easily be understood that all terms that do not involve S_m will generate series that are absolutely convergent due to the factorial growth outpacing any exponential growth. The radius of convergence of the first three terms is zero. Therefore:

$$\sum_{m=0}^{\infty}|d_1| < \infty, \ \sum_{m=0}^{\infty}|d_2| < \infty, \ \sum_{m=0}^{\infty}|d_3| < \infty. \tag{B7}$$

To prove the three remaining terms also absolutely converge, we first notice that, for $m \to \infty$, the following expansions hold true:

$$\operatorname{Re}\{C_m \operatorname{erfi}(C_m)\} = -C_2\sqrt{m} + e^{-C_2^2 m}\frac{\cos(2C_1C_2)}{\sqrt{\pi}}\left[1 + \mathcal{O}\left(\frac{1}{m}\right)\right], \tag{B8}$$

$$\operatorname{Re}\{C_m\}\operatorname{erfi}(\operatorname{Re}\{C_m\}) = \frac{2C_1}{\sqrt{\pi}m} + \mathcal{O}\left(\frac{1}{m}\right)^2, \tag{B9}$$

Thus we see that S_m grows *at worst* as $\sqrt{m}$ and S_m^2 as m. Therefore, replacing S_m into (B5), and using similar argument than previously, we can see that the radius of convergence of the last three terms is also zero, from which we conclude:

$$\sum_{m=0}^{\infty}|d_4| < \infty, \ \sum_{m=0}^{\infty}|d_5| < \infty, \ \sum_{m=0}^{\infty}|d_6| < \infty. \tag{B10}$$

---

[2] The d'Alembert criterion states that if $r \equiv \lim_{n\to\infty}|a_{n+1}/a_n| < 1$, then $\sum_{n=0}^{\infty} a_n$ absolutely converges, with r being convergence radius.
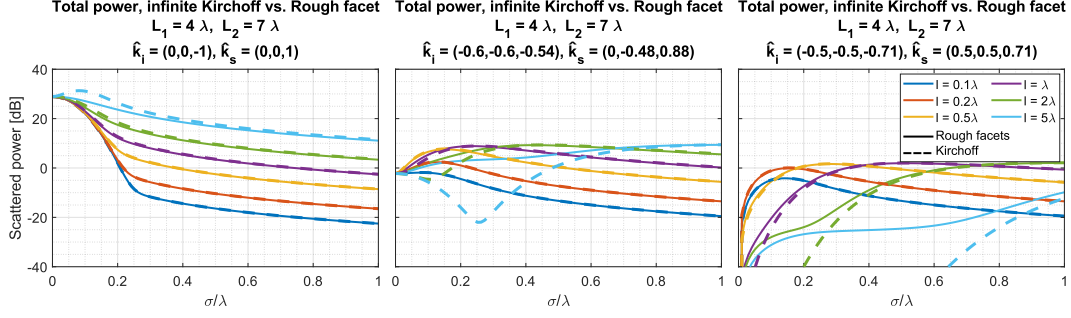
Figure B1: Comparison between the rough facet formulation (this work), and the infinite-terrain backscattering law, using an identical setup as for the facet-level validation presented in Section 4.1 and Figure 4. Solid lines: Rough facet total power $\langle|\Phi|^2\rangle = |\langle\tilde{\Phi}\rangle|^2 + D_\Phi$. Dashed lines: Kirchoff backscattering function $\langle|\Phi|^2\rangle = |\langle\tilde{\Phi}\rangle|^2 + \sigma_K$.

By virtue of (B2) we have proved that D_Φ is not only convergent, but absolutely for any choice of parameters.

In practice, we have found that the series generally converges with as little as 10 terms for gentle amounts of roughness ($\sigma \lesssim \lambda/20$) and as much as 250 terms when σ is comparable to the wavelength. The correlation length l and the bistatic angles of scattering have a moderate effect on the number of terms needed for convergence.

Appendix C Comparison with Kirchoff backscattering law

The novel formula (21) can be regarded as the finite-facet equivalent of the Kirchoff incoherent backscattering function derived in (Kong, 2000) and other textbooks, given by

$$\sigma_K = \pi L_x L_y \sum_{m=1}^{\infty} \frac{(\sigma^2 K^2)^m}{m!m} l^2 e^{\frac{-K_\rho^2 l^2}{4m}} e^{-\sigma^2 K^2}, \tag{C1}$$

where $K_\rho^2 = k_{d,x}^2 + k_{d,y}^2$. While the derivation of (C1) sends the bounds of (A8) to infinity –or equivalenty, invokes an $l \ll L$ assumption–, the rough facet formulation invokes no such assumption and preserves the original facet dimensions. Naturally, the correlation length in the rough facet formulation cannot be infinitely large with respect to the facet dimensions but the limitation arises from the physical meaning of having $l \gg L$ rather than being built-in the formula. The practical consequence of this is that the range of validity of the rough facet formula is greater in the (σ, l, L) space.

In Figure B1 we compare the rough-facet total power to the Kirchoff total power for the same cases as those analysed in Figure 4. Since the rough-facet curves of Figure 4 were in excellent agreement with the data points, we can interpret any deviation of Kirchoff from the rough facets as erroneous.

The Kirchoff backscattering law is in very good agreement with the rough facet formulation for either very small correlation lengths, or very large RMS heights. Differences appear outside of this regime. We can observe that for nadir backscattering, significant deviation start to appear at low σ values when $l = 5\lambda$, for a facet that is 4λ by 7λ of size. For larger look angles, > 10 dB deviations occur at $l = 2\lambda$, or even $l = \lambda$ for very small RMS heights ($\sigma < 0.1\lambda$). Overall, (C1) can severely break down as early as $l \approx 0.2L$ for some combinations of σ and scattering angles, while the rough facet formula easily maintained accuracy at $l \sim L$ for all angles and all values of σ.

In conclusion, the rough-facet formula allows for greater flexibility in the choice of facet-level roughness parameters than the Kirchoff backscattering function. Leaving more room for a geophysics-driven choice of small-scale roughness, rough facets are better-suited for integration in a facet method-based radar simulator.

Appendix D Equivalence of average incoherent power and speckle

We provide a quick proof the that inclusion of speckle in Section 3.3 gives that correct average power. Using the following shorthand, let the coherent, incoherent, and total fields from a single facet be

$$U_{\text{coh}} = \langle \tilde{\Phi} \rangle, \tag{D1}$$

$$U_{\text{incoh}} = \sqrt{D_\Phi} \phi_r, \tag{D2}$$

$$U_{\text{tot}} = U_{\text{coh}} + U_{\text{incoh}}, \tag{D3}$$

where ϕ_r is given by (25). The total average power is

$$P = \langle |U_{\text{tot}}|^2 \rangle. \tag{D4}$$

Substituting the above we get

$$P = \langle |U_{\text{coh}} + U_{\text{incoh}}|^2 \rangle, \tag{D5}$$

$$= \langle |U_{\text{coh}}|^2 + 2\,\text{Re}\,\{U_{\text{coh}} U_{\text{incoh}}\} + |U_{\text{incoh}}|^2 \rangle, \tag{D6}$$

$$= \langle |U_{\text{coh}}|^2 \rangle + \langle 2\,\text{Re}\,\{U_{\text{coh}} U_{\text{incoh}}\} \rangle + \langle |U_{\text{incoh}}|^2 \rangle, \tag{D7}$$

$$= |U_{\text{coh}}|^2 + \langle |U_{\text{incoh}}|^2 \rangle, \tag{D8}$$

where we have used the fact that U_{coh} is a constant and the real and imaginary parts of ϕ_r are zero-mean Gaussian random variables which eliminates the cross term. Looking at the incoherent component and substituting (D2) and (25)

$$\langle |U_{\text{incoh}}|^2 \rangle = \langle |\sqrt{D_\Phi} \phi_r|^2 \rangle, \tag{D9}$$

$$= D_\Phi \langle |\varepsilon_1 + i\varepsilon_2|^2 \rangle / 2, \tag{D10}$$

$$= D_\Phi \left(\langle |\varepsilon_1|^2 \rangle + \langle |\varepsilon_2|^2 \rangle \right) / 2, \tag{D11}$$

$$= D_\Phi (1 + 1) / 2, \tag{D12}$$

$$= D_\Phi, \tag{D13}$$

where we have used the fact that the mean of the square of the standard normal $\mathcal{N}(0, 1)$ is equal to 1. Therefore, this speckle model gives the same average power as summing the average coherent and average incoherent powers alone, that is

$$P = |\langle \tilde{\Phi} \rangle|^2 + D_\Phi. \tag{D14}$$

References

Abramowitz, M., & Stegun, I. A. (1964). *Handbook of mathematical functions with formulas, graphs, and mathematical tables* (Vol. 55). US Government printing office.

Berquin, Y., et al. (2015). Computing low-frequency radar surface echoes for planetary radar using huygens-fresnel's principle. *Radio Science*, *50*(10), 1097–1109. Retrieved from http://dx.doi.org/10.1002/2015RS005714 (2015RS005714) doi: 10.1002/2015RS005714

Blankenship, D., Ray, T., Plaut, J., Moussessian, A., Patterson, W., Romero-Wolf, A., ... others (2018). Reason for europa. *42nd COSPAR Scientific Assembly*, *42*, B5–3.

Botev, Z. (2016). *Fractional brownian field or surface generator.* MATLAB Central file exchange. Retrieved from `https://nl.mathworks.com/matlabcentral/fileexchange/38945-fractional-brownian-field-or-surface-generator`

Botev, Z. (2022). *Circulant embedding method for generating stationary gaussian field.* MATLAB Central file exchange. Retrieved from `https://nl.mathworks.com/matlabcentral/fileexchange/38880-circulant-embedding-method-for-generating-stationary-gaussian-field`

Bruzzone, L., Bovolo, F., Thakur, S., Carrer, L., Donini, E., Gerekos, C., ... Sbalchiero, E. (2020). Envision mission to venus: Subsurface radar sounding. In *Igarss 2020-2020 ieee international geoscience and remote sensing symposium* (pp. 5960–5963).

Bruzzone, L., Plaut, J. J., Alberti, G., Blankenship, D. D., Bovolo, F., Campbell, B. A., ... others (2013). Rime: Radar for icy moon exploration. In *2013 ieee international geoscience and remote sensing symposium-igarss* (pp. 3907–3910).

Cai, Y., & Fa, W. (2020). Meter-scale topographic roughness of the moon: The effect of small impact craters. *Journal of Geophysical Research: Planets*, *125*(8), e2020JE006429.

Campbell, B. A., & Shepard, M. K. (2003). Coherent and incoherent components in near-nadir radar scattering: Applications to radar sounding of mars. *Journal of Geophysical Research: Planets*, *108*(E12).

Carrer, L., Gerekos, C., Bovolo, F., & Bruzzone, L. (2019). Distributed radar sounder: A novel concept for subsurface investigations using sensors in formation flight. *IEEE Transactions on Geoscience and Remote Sensing*, *57*(12), 9791–9809.

Castelletti, D., Schroeder, D. M., Mantelli, E., & Hilger, A. (2019). Layer optimized sar processing and slope estimation in radar sounder data. *Journal of Glaciology*, *65*(254), 983–988.

Chu, W., Schroeder, D. M., Seroussi, H., Creyts, T. T., & Bell, R. E. (2018). Complex basal thermal transition near the onset of petermann glacier, greenland. *Journal of Geophysical Research: Earth Surface*, *123*(5), 985–995.

Croci, R., Seu, R., Flamini, E., & Russo, E. (2011). The shallow radar (sharad) onboard the nasa mro mission. *Proceedings of the IEEE*, *99*(5), 794–807.

Dente, L., Guerriero, L., Comite, D., & Pierdicca, N. (2020). Space-borne gnss-r signal over a complex topography: Modeling and validation. *IEEE Journal of Selected Topics in Applied Earth Observations and Remote Sensing*, *13*, 1218–1233.

Fa, W., & Jin, Y. (2010). Simulation of radar sounder echo from lunar surface and subsurface structure. *Science China Earth Sciences*, *53*(7), 1043–1055.

Fergason, R., Hare, T., & Laura, J. (2018). Hrsc and mola blended digital elevation model at 200m v2. *Astrogeology PDS Annex, US Geological Survey*.

Ferro, A. (2019). Squinted sar focusing for improving automatic radar sounder data analysis and enhancement. *International Journal of Remote Sensing*, *40*(12), 4762–4786.

Fung, A. K. (1994). Microwave scattering and emission models and their applications. *Norwood, MA: Artech House, 1994.*.

Gerekos, C. (2020). *Advanced backscattering simulation methods for the design of spaceborne radar sounders.* Doctoral dissertation, Università degli Studi di Trento.

Gerekos, C., Bruzzone, L., & Imai, M. (2019). A coherent method for simulating active and passive radar sounding of the jovian icy moons. *IEEE Transactions on Geoscience and Remote Sensing*, *58*(4), 2250–2265.

Gerekos, C., Tamponi, A., Carrer, L., Castelletti, D., Santoni, M., & Bruzzone, L. (2018). A coherent multilayer simulator of radargrams acquired by radar sounder instruments. *IEEE Transactions on Geoscience and Remote Sensing*,

56(12), 7388–7404.

Grima, C., Blankenship, D. D., Young, D. A., & Schroeder, D. M. (2014). Surface slope control on firn density at thwaites glacier, west antarctica: Results from airborne radar sounding. *Geophysical Research Letters*, *41*(19), 6787–6794.

Grima, C., Schroeder, D. M., Blankenship, D. D., & Young, D. A. (2014). Planetary landing-zone reconnaissance using ice-penetrating radar data: Concept validation in antarctica. *Planetary and Space Science*, *103*, 191–204.

Haynes, M. S. (2019). Homodyned-k distribution with additive gaussian noise. *IEEE Transactions on Aerospace and Electronic Systems*, *55*(6), 2992–3002.

Haynes, M. S., Chapin, E., & Schroeder, D. M. (2018). Geometric power fall-off in radar sounding. *IEEE Transactions on Geoscience and Remote Sensing*, *56*(11), 6571–6585.

Heggy, E., Scabbia, G., Bruzzone, L., & Pappalardo, R. T. (2017). Radar probing of jovian icy moons: Understanding subsurface water and structure detectability in the juice and europa missions. *Icarus*, *285*, 237–251.

Heister, A., & Scheiber, R. (2018). Coherent large beamwidth processing of radio-echo sounding data. *The Cryosphere*, *12*(9), 2969–2979.

Iodice, A., Natale, A., & Riccio, D. (2012). Kirchhoff scattering from fractal and classical rough surfaces: Physical interpretation. *IEEE Transactions on Antennas and Propagation*, *61*(4), 2156–2163.

Jordan, R., Picardi, G., Plaut, J., Wheeler, K., Kirchner, D., Safaeinili, A., . . . others (2009). The mars express marsis sounder instrument. *Planetary and Space Science*, *57*(14-15), 1975–1986.

Kobayashi, T., Oya, H., & Ono, T. (2002). B-scan analysis of subsurface radar sounding of lunar highland region. *Earth, planets and space*, *54*(10), 983–991.

Kong, J. A. (2000). *Electromagnetic wave theory.* EMW Publishing.

Landais, F., Schmidt, F., & Lovejoy, S. (2015). Universal multifractal martian topography. *Nonlinear Processes in Geophysics*, *22*(6), 713–722.

Lei, Y., Haynes, M. S., Arumugam, D., & Elachi, C. (2020). A 2-d pseudospectral time-domain (pstd) simulator for large-scale electromagnetic scattering and radar sounding applications. *IEEE Transactions on Geoscience and Remote Sensing*, *58*(6), 4076–4098.

MacGregor, J., Matsuoka, K., & Studinger, M. (2009). Radar detection of accreted ice over lake vostok, antarctica. *Earth and Planetary Science Letters*, *282*(1-4), 222–233.

MacKie, E., Schroeder, D., Caers, J., Siegfried, M., & Scheidt, C. (2020). Antarctic topographic realizations and geostatistical modeling used to map subglacial lakes. *Journal of Geophysical Research: Earth Surface*, *125*(3), e2019JF005420.

Nouvel, J.-F., Herique, A., Kofman, W., & Safaeinili, A. (2004). Radar signal simulation: Surface modeling with the facet method. *Radio Science*, *39*(1), 1–17.

Ono, T., Kumamoto, A., Kasahara, Y., Yamaguchi, Y., Yamaji, A., Kobayashi, T., . . . others (2010). The lunar radar sounder (lrs) onboard the kaguya (selene) spacecraft. *Space Science Reviews*, *154*(1), 145–192.

Ono, T., Kumamoto, A., Nakagawa, H., Yamaguchi, Y., Oshigami, S., Yamaji, A., . . . Oya, H. (2009). Lunar radar sounder observations of subsurface layers under the nearside maria of the moon. *Science*, *323*(5916), 909–912.

Oswald, G., & Gogineni, S. (2008). Recovery of subglacial water extent from greenland radar survey data. *Journal of Glaciology*, *54*(184), 94–106.

Raney, R. K. (2011). Cryosat sar-mode looks revisited. *IEEE Geoscience and Remote Sensing Letters*, *9*(3), 393–397.

Rutishauser, A., Blankenship, D. D., Sharp, M., Skidmore, M. L., Greenbaum, J. S., Grima, C., . . . Young, D. A. (2018). Discovery of a hypersaline subglacial lake complex beneath devon ice cap, canadian arctic. *Science advances*, *4*(4), eaar4353.

Sbalchiero, E., Thakur, S., Cortellazzi, M., & Bruzzone, L. (2021). A novel integrated radar sounder simulation technique for modelling large and small-scale surface scattering phenomena. In *Image and signal processing for remote sensing xxvii* (Vol. 11862, pp. 222–234).

Schroeder, D. M., Bingham, R. G., Blankenship, D. D., Christianson, K., Eisen, O., Flowers, G. E., ... Siegert, M. J. (2020). Five decades of radioglaciology. *Annals of Glaciology*, *61*(81), 1–13.

Schroeder, D. M., Blankenship, D. D., Raney, R. K., & Grima, C. (2014a). Estimating subglacial water geometry using radar bed echo specularity: application to thwaites glacier, west antarctica. *IEEE Geoscience and Remote Sensing Letters*, *12*(3), 443–447.

Schroeder, D. M., Blankenship, D. D., Raney, R. K., & Grima, C. (2014b). Estimating subglacial water geometry using radar bed echo specularity: application to thwaites glacier, west antarctica. *IEEE Geoscience and Remote Sensing Letters*, *12*(3), 443–447.

Schroeder, D. M., Blankenship, D. D., & Young, D. A. (2013). Evidence for a water system transition beneath thwaites glacier, west antarctica. *Proceedings of the National Academy of Sciences*, *110*(30), 12225–12228.

Smith, D. E., Zuber, M. T., Neumann, G. A., Lemoine, F. G., Mazarico, E., Torrence, M. H., ... others (2010). Initial observations from the lunar orbiter laser altimeter (lola). *Geophysical Research Letters*, *37*(18).

Tsang, L., & Kong, J. A. (2004). *Scattering of electromagnetic waves: advanced topics.* John Wiley & Sons.

Ulaby, F. T., Moore, R. K., & Fung, A. K. (1981). Microwave remote sensing: Active and passive. volume 1-microwave remote sensing fundamentals and radiometry.

Weisstein, E. W. (2022). Erfi. *https://mathworld. wolfram. com/*.

Wright, A., & Siegert, M. (2012). A fourth inventory of antarctic subglacial lakes. *Antarctic Science*, *24*(6), 659–664.

Xu, H., Zhu, J., Tsang, L., & Kim, S. B. (2021). A fine scale partially coherent patch model including topographical effects for gnss-r ddm simulations. *Progress in electromagnetics research*, *170*, 97–128.